

Numerical modelling of fracturing processes during cold water injection into geothermal reservoirs

Verification and qualitative validation

Luo, Wen; Liaudat, Joaquín; Ouf, Josselin; Dieudonné, Anne Catherine; Amann, Florian; Vardon, Philip J.

DOI

[10.1016/j.compgeo.2025.107186](https://doi.org/10.1016/j.compgeo.2025.107186)

Publication date

2025

Document Version

Final published version

Published in

Computers and Geotechnics

Citation (APA)

Luo, W., Liaudat, J., Ouf, J., Dieudonné, A. C., Amann, F., & Vardon, P. J. (2025). Numerical modelling of fracturing processes during cold water injection into geothermal reservoirs: Verification and qualitative validation. *Computers and Geotechnics*, 183, Article 107186.

<https://doi.org/10.1016/j.compgeo.2025.107186>

Important note

To cite this publication, please use the final published version (if applicable).
Please check the document version above.

Copyright

Other than for strictly personal use, it is not permitted to download, forward or distribute the text or part of it, without the consent of the author(s) and/or copyright holder(s), unless the work is under an open content license such as Creative Commons.

Takedown policy

Please contact us and provide details if you believe this document breaches copyrights.
We will remove access to the work immediately and investigate your claim.



Research paper

Numerical modelling of fracturing processes during cold water injection into geothermal reservoirs: Verification and qualitative validation

Wen Luo ^{a,b},* , Joaquín Liaudat ^c, Josselin Ouf ^{a,b}, Anne-Catherine Dieudonné ^a, Florian Amann ^b, Philip J. Vardon ^a

^a Faculty of Civil Engineering and Geosciences, Delft University of Technology, Delft, 2628 CN, The Netherlands

^b Department of Engineering Geology and Hydrogeology, RWTH Aachen, Aachen, D-52064, Germany

^c Institute of Geotechnics, Department of Civil and Environmental Engineering, Technical University of Darmstadt, Darmstadt, D-64287, Germany



ARTICLE INFO

Keywords:

Fracturing
Thermo-hydro-mechanics
Geothermal energy
Cohesive zone model

ABSTRACT

Cold water injection into geothermal reservoirs is a common, sometimes necessary, technique for multiple reasons including the replenishment and stimulation of the reservoirs, and the disposal of waste water. The injection of cold water results in a thermo-hydro-mechanical (THM) impulse, which can cause near-wellbore cracking. A method is presented to simulate coupled thermo-hydro-mechanical processes, including the re-activation of existing fractures and fracturing of the rock matrix. The model is based on the finite element method, and utilises a newly developed cohesive interface element to represent discontinuities. The interface element belongs to the family of zero-thickness elements and is triple-noded. It is developed to allow the simulation of longitudinal and transversal fluid/heat flow. The cubic law is used to simulate the fracture transmissivity as a function of its aperture, while a elasto-damage law is used to characterise the mechanical response of the discontinuity. The method is successfully verified against analytical solutions for hydraulic fracturing (KGD model) and for the thermo-hydraulic response of a single fracture (Lauwerier's problem). As numerical oscillations are observed due to the high Péclet number, an artificial diffusion is added to stabilise the numerical solution with sufficient accuracy. Qualitative validation is achieved against experimental data of cold water injection in granite samples. Fracture branching is observed in the case with large cooling shock, while a single fracture is induced in the case with smaller cooling shock, as was observed in the experiment. The validation demonstrates the capability of the proposed model to simulate fracturing processes under THM couplings.

1. Introduction

The exploitation of geothermal energy is gaining increasing popularity and is recognised as a vital element in achieving climate targets (European Commission, 2023). Hot water is extracted from a subsurface reservoir, and useful energy is obtained from it. To maintain the production rate and manage the disposal of the produced water, the injection of cold water back into the reservoir is a common practice. The injection of cold water causes a significant local thermo-hydro-mechanical (THM) and sometimes chemical perturbation. This can cause both advantageous and disadvantageous impacts (Luo et al., 2023). It has been commonly assumed that injection of cold water leads to an increase of pressure to maintain injection rates (primarily due to increased viscosity) (Veldkamp et al., 2016). However, field data have also shown unintentional injectivity enhancement during injection, such as during injection into Wells A-7 & A-8 in Los Azufres field,

Mexico (Benson et al., 1987), BR7 & BR13 in Broadlands field, New Zealand (Horne, 1982), HN-09 in Hellisheiði field Iceland (Gunnarsson, 2011), and OK-2 in Southern Negros field and 4R1 in Tongonan field, both in Philippines (Dobbie et al., 1982). In a recent review on the main processes underlying cold water injection, it is concluded that the formation of new fractures and/or re-activation of pre-existing fractures in the near-field of injection well bores can be a major contributor to the observed injectivity improvement (Luo et al., 2023).

Understanding how the fracturing processes are influenced by the coupled THM processes resulting from (re-)injection, and how the injection performance is influenced by the fracture characteristics and behaviour, is therefore crucial for designing and managing operations. Analytical studies are generally restricted to simple 1D problems in an idealised geometry, e.g., studies on optimising heat extraction from enhanced geothermal systems (EGS) (Akdas and Onur, 2022; Fox et al.,

* Corresponding author at: Faculty of Civil Engineering and Geosciences, Delft University of Technology, Delft, 2628 CN, The Netherlands.
E-mail address: W.Luo@tudelft.nl (W. Luo).

2016), or combined with field data to derive empirical relationships between injection temperature and injectivity (Grant et al., 2013).

Thanks to the rapid development of high-performance computation, more complex and coupled processes can be studied with a more realistic description of the subsurface and its evolution. Multiple advanced codes have been used to study mainly coupled thermo-hydraulic processes and transport phenomena in complex subsurface structures, such as TOUGH2 (Doughty, 2013), MRST-AD (Krogstad et al., 2015), FEHM (Zyvoloski, 2007), AD-GPRS (Garipov et al., 2018), and DARTS (Wang et al., 2020). While the focus of these codes is on the strong couplings between multi-phase flow, transport phenomena, and phase changes, the description of fluid-rock interactions is essential for geothermal engineering in which the behaviour of rock/fractures plays a crucial role. Several codes, such as OpenGeoSys (Kolditz et al., 2012), GEOX (Settgast, 2022), MOOSE-based codes (Dudani et al., 2014; Podgorney et al., 2021; Jacquey, 2017), UDEC (Israelsson, 1996), DRAC (Pérez Carreras, 2018), and LAGAMINE (Charlier, 1987; Collin, 2003) have been developed to simulate fully coupled thermo-hydro-mechanical processes in the subsurface, each employing various approaches to tackle simulations involving discontinuities.

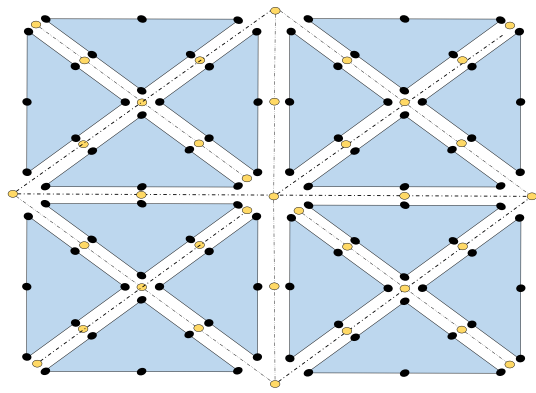
Two main categories of numerical approaches have been proposed and developed to solve problems which include discontinuities, namely continuous and discrete numerical methods. The former category includes methods like the Finite Difference Method (FDM), Finite Element Method (FEM) and Boundary Element Method (BEM), and treats the rock as an equivalent continuum with the discontinuities being either implicitly or explicitly represented. In contrast, the Discrete Element Method (DEM, including Distinct Element Method, Discontinuous Deformation Analysis and Bounded Particle Method) treats the rock as an assemblage of particles or blocks, so that discontinuities are explicitly considered. Although DEM allows larger displacements and rotations of discrete elements, it is not able to solve flow and heat transfer problems by its own. Also, its high demand of computational resources to calculate the interactions between particles or blocks limits the application to small-scale problems. In addition, significant uncertainties can be introduced as it is challenging to model realistic particle geometries and to determine the material parameters required to define the mechanical relationships between the particles (Min, 2013). Therefore, continuous numerical methods, typically FEM (which has advantages over FDM and BEM in terms of efficiency in handling non-linear processes and capability of describing complex boundary geometries Min, 2013) remain the most popular numerical methods to simulate multi-physics problems including discontinuities, despite challenges in incorporating them into meshes.

The simulation of discontinuous problems can be performed with different techniques based on FEM, such as Element Deletion Method (Livermore Software Technology, 2007), Adaptive Element Method (Schrefler et al., 2006), Extended Finite Element Method (XFEM) (Jafari et al., 2023), cohesive interface elements (Settgast et al., 2017; Lequesne et al., 2006; Dieudonné et al., 2015; Cerfontaine et al., 2015; Liaudat et al., 2023), and Phase Field Method (PFM) (Lepillier et al., 2020). Among the proposed approaches, cohesive interface element, combined with cohesive zone model (CZM), is the dominant choice in modelling fracturing processes using FEM (Nguyen et al., 2017), due to its mitigation of the need to calculate the stress singularity at the fracture tips that is commonly challenging in methods based on linear elastic fracture mechanics (e.g., XFEM) (Min, 2013; Nguyen et al., 2017) and its clear physical meaning. In addition, unlike XFEM (Min, 2013; Wu et al., 2020), cohesive interface element is capable of modelling fracture nucleation and initiation (Nguyen et al., 2017). Although the phase-field method can also avoid the challenges in stress singularities, finer meshes with dimensions smaller than the so-called length-scale parameter are required, resulting in a high computational cost (Dally et al., 2020).

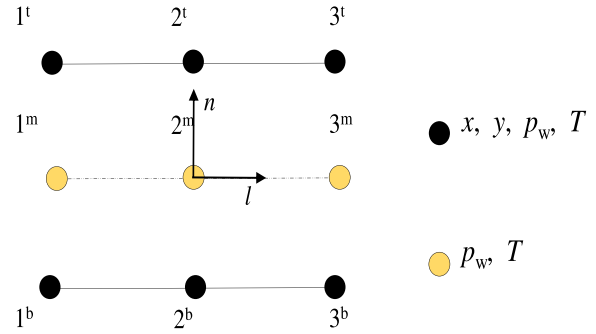
Cohesive zone model was first proposed by Dugdale (1960) and Barenblatt (1962) to circumvent the unrealistic infinite stresses at the

fracture tip obtained for a linear elastic material, assuming a cohesive-law-governed zone in front of the fracture tip. Later, Hillerborg et al. (1976) introduced CZM into FEM to simulate crack initiation and growth in concrete. When discretising the material domain, the material separation and thus damage of the structure can be described by interface elements in-between continuum elements (Scheider, 2001), governed by the cohesive law that relates traction and separation of the two surfaces of the interface element. Due to the advantages mentioned earlier, the cohesive interface elements have been widely applied to modelling hydraulic fracturing (Nguyen et al., 2017), fault slip (Van Den Bogert, 2015), the behaviour of soil–structure interfaces (Cerfontaine et al., 2015) and gas fracturing in clay barriers (Liaudat et al., 2023). However, most of the previous research only considered hydro-mechanical or pneumo-hydro-mechanical couplings (Liaudat et al., 2023; Dieudonné, 2016; Nguyen et al., 2017; Lu et al., 2013; Carrier and Granet, 2012). As heat transfer and thermal stresses play a key role in extracting geothermal energy, fully coupled THM processes are necessary to be considered in the model. A limited number of previous works considered heat transfer in interface elements, for example, Alonso et al. (2013), Pérez Carreras (2018) and Cui et al. (2019) considered heat transfer in interface elements, but with a double node scheme, which does not allow the consideration of the temperature and fluid pressure inside the discontinuity independently from the adjacent continuum elements, although has a simpler formulation. The temperature and pressure at the middle of the interface requires assumptions, e.g., taking the average value between the bottom and top faces of the interface. It has been demonstrated that in certain circumstances the double-node scheme can introduce errors that depend on the longitudinal temperature/pressure profile, hydraulic/diffusion coefficients and thus on mechanical processes (Liaudat et al., 2023). In contrast, the triple-node scheme (Fig. 1(b)) allows a more “flexible” representation of the transversal fluid and heat flow between the interface element and the surrounding continuum elements. Therefore, such interface elements can be used for applications where an explicit representation of the mid-plane pressure and temperature is convenient, such as the interfaces between permeable and impermeable materials. In addition, the mechanical laws implemented in the interface elements of previous works reflect the targeted physical process, with for example, the work of Cui et al. (2019) and Ranjbar et al. (2020) not including damage processes and Alonso et al. (2013) not updating stiffness with damage. Since the problems considered in their works were always in compression and mode I fracture is not considered, the thermo-mechanical and hydro-mechanical couplings were moderate. Furthermore, in their modelling exercises, the shearing path was prescribed along a pre-defined line and the cases where the fractures can choose the most efficient fracturing paths were not discussed.

In this work, a fully coupled THM model using zero-thickness and triple-noded interface elements is developed on the basis of existing literature (Collin, 2003; Lequesne et al., 2006; Liaudat et al., 2023). Heat conduction and convection are allowed in both longitudinal and transversal directions of the interface element, with stabilisation used for cases with high Péclet number. An elasto-damage law is used to characterise the mechanical response of the discontinuity, allowing the opening of the interface elements. This, in turn, leads to strong coupling, as the longitudinal hydraulic conductivity of the interface elements evolves with the opening. In addition, a node-to-node contact approach is used to pre-determine the contact faces of the interface elements, thus assuring that the contact faces are pre-determined and accelerating computation, particularly when interface elements are inserted in between all the continuum elements, as discussed in the validation example. Compared to the previous work by Liaudat et al. (2023), the current work expands the application of the proposed method for geothermal reservoirs and other cases where coupled THM processes in discontinuities play a key role. In addition, the substantial verification and validation implemented in this work demonstrates the performance of the developed method. The structure of this paper is as



(a) Insertion of interface elements in between continuum elements.



(b) Interface element

Fig. 1. Finite elements used. (a) Interface elements in between continuum elements to represent pre-existing or potential cracking paths, and (b) Element node numbering, nodal degrees of freedom and local basis.

follows: first, a brief introduction to zero-thickness interface elements within FEM is presented, followed by the mathematical formulations for both continuous and discontinuous media. Subsequently, the code is verified against coupled thermo-hydraulic and hydro-mechanical analytical solutions to demonstrate its accuracy, after which the proposed method is validated against experimental results from a near-borehole thermal fracturing experiment conducted by Zhang et al. (2019).

2. Numerical model

2.1. Modelling approach

Modelling fracture behaviour in continuous porous media (e.g., rock) is a non-trivial task, as discontinuities break displacement compatibility of standard FEM formulations and pose strong singularities in the solutions. To mitigate these difficulties, zero-thickness interface elements, a conceptually simple technique, are used to represent the discontinuities in this work. Interface elements are inserted in between continuum elements to represent pre-existing or potential fractures, as is shown in Fig. 1. A 2D modelling approach is used, with each interface element having in total 9 nodes, equally distributed on top, mid, and bottom planes (Fig. 1(b)). For an unloaded interface element, these three planes coincide in the same position. That means, for instance, that nodes 1^t , 1^m , and 1^b have initially the same coordinates. This is why this element is called a zero-thickness and triple-nodded interface element.

The bottom and top faces of the interface element share nodes with the continuum element with four degrees of freedom corresponding to coordinates x , and y , water pressure p_w , and temperature T , while the mid-plane nodes have only degrees of freedom of water pressure p_w and temperature T . In this way, different constitutive laws can be used for the continuum and the discontinuities, allowing for a more realistic representation of the heat and fluid flows along and across the fracture. The nodes of the bottom and top faces of the interface which are in contact with each other are pre-determined to both improve robustness and decrease computation. This, however, reduces the amount of shear displacement possible.

In a previous work, Liaudat et al. (2023) developed a Pneumo-Hydro-Mechanical Interface (PHMI) element to simulate gas fracturing in saturated clay samples under isothermal conditions. In the present paper, the PHMI element is further developed to take into account thermal processes under the assumptions that the material is always water saturated (i.e., without considering a gas phase). Additionally, the water properties (e.g., density and thermal conductivity) are assumed to be linearly proportional to temperature change. In the following

section, the mathematical formulations for both the continuum and discontinuities are described. The newly developed formulations have been implemented into the FEM code LAGAMINE (Charlier, 1987), in which the formulation of continuum was implemented by Collin et al. (2002).

2.2. Governing equations for the continuum porous medium

The governing equations follow the formulation proposed by Collin et al. (2002) Here the equations with corresponding constitutive laws are briefly introduced.

2.2.1. Hydraulic problem

The water mass balance equation without any internal source or sink reads as follows::

$$\frac{\partial(\phi\rho_w)}{\partial t} + \nabla \cdot (\rho_w \mathbf{v}_w) = 0 \quad (1)$$

where ρ_w [kg/m³] is the water density, ϕ the porosity, and \mathbf{v}_w [m/s] the Darcy velocity vector. The latter is in turn defined as:

$$\mathbf{v}_w = -\frac{\mathbf{K}}{\mu} \nabla p_w \quad (2)$$

where \mathbf{K} [m²] is the intrinsic permeability tensor, μ [Pa s] is the water dynamic viscosity, and p_w [Pa] is the water pressure.

2.2.2. Mechanical problem

If equilibrium state is assumed and if gravity is neglected, the equation of momentum conservation reads as follows:

$$\nabla \cdot \boldsymbol{\sigma} = \mathbf{0} \quad (3)$$

where $\boldsymbol{\sigma}$ [Pa] is the Cauchy's total stress tensor.

The considered mechanical constitutive law for the bulk rock is the classical law (Jaeger et al., 2009). If compressive stress and strain are defined as negative, the thermo-poro-elastic constitutive law reads as follows:

$$\Delta\boldsymbol{\sigma} = \mathbb{C} : \Delta\boldsymbol{\epsilon} - \alpha\Delta p_w \mathbf{I} - \beta_b K_b \Delta T \mathbf{I} \quad (4)$$

where \mathbb{C} is the 4th-order elastic stiffness tensor, $\boldsymbol{\epsilon}$ is the strain tensor, α is the Biot coefficient, \mathbf{I} is the 2nd-order identity tensor, β_b is the bulk volumetric thermal expansion coefficient, and K_b [Pa] is the drained bulk modulus.

2.2.3. Thermal problem

Under the assumption of local thermal equilibrium, with no internal source or sink, the equation of energy conservation reads:

$$\frac{\partial[(\rho c_p)_b T]}{\partial t} + \nabla \cdot \mathbf{q}_T = 0 \quad (5)$$

where, $(\rho c_p)_b = (1 - \phi)(\rho c_p)_s + \phi(\rho c_p)_w$ is the bulk volumetric heat capacity (with c_p [J/(kg K)] being the phase specific heat capacity, ρ the phase density, and the subscripts s and w referring to the solid and the water phases, respectively), and \mathbf{q}_T [J/(m² s)] is the heat flux vector. The latter is obtained from the following expression:

$$\mathbf{q}_T = -\lambda_b \nabla T + \rho_w c_{pw} \mathbf{q}_D T \quad (6)$$

where the first term corresponds to Fourier's law with the bulk thermal conductivity given by λ_b [J/(m s K)] = $(1 - \phi)\lambda_s + \phi\lambda_w$, and the second term corresponds to the heat advection due to water flow.

2.3. Governing equations for the discontinuities

The mechanical and hydraulic governing equations for the interface elements are inherited from Liaudat et al. (2023) with the gas phase being neglected. Additionally, the governing equations for thermal processes are included here. Note that the following equations are tailored for 2D problems.

2.3.1. Hydraulic problem

The mass balance for water in a differential volume of discontinuity $w dl$ reads:

$$\frac{\partial}{\partial t}(w \rho_w) + \frac{\partial q_w^l}{\partial l} - q_w^b - q_w^t = 0 \quad (7)$$

where w [m] is the width of the discontinuity, q_w^l [kg/(m s)] is the longitudinal water mass flow, and q_w^b and q_w^t [kg/(m² s)] are the transversal water mass flows incoming to the discontinuity from surrounding continuum medium (Liaudat et al., 2023).

The mass flows in Eq. (7) can be expanded as:

$$q_w^l = \rho_w v_w^l; \quad q_w^b = \rho_w v_w^b; \quad q_w^t = \rho_w v_w^t \quad (8)$$

where v_w^l [m²/s], v_w^b [m/s] and v_w^t [m/s] are the longitudinal and transversal (top and bottom) volumetric flows. These flows obtained from the following generalised Darcy's law:

$$v_w^l = -\frac{l^1}{\mu_w} \frac{\partial p_w^m}{\partial l}; \quad v_w^b = -\frac{k^b}{\mu_w} \check{p}_w^b; \quad v_w^t = -\frac{k^t}{\mu_w} \check{p}_w^t \quad (9)$$

where l^1 [m³] is the longitudinal hydraulic coefficient, k^b [m²] and k^t [m²] are the transversal permeability of the interface, p_w^m [Pa] is the water pressure at the middle plane, and \check{p}_w^b [Pa] and \check{p}_w^t [Pa] are the transversal pressure jumps between the bottom and top face and the mid-plane, respectively. The transversal pressure drops are defined as follows:

$$\check{p}_w^b = (p_w^m - p_w^b); \quad \check{p}_w^t = (p_w^m - p_w^t) \quad (10)$$

where p_w^b and p_w^t are the water pressures at the bottom and top sides of the discontinuity.

The longitudinal hydraulic coefficient l^1 is estimated using the Reynolds lubrication equation, which describes the laminar flow of an incompressible and Newtonian fluid flowing between two parallel plates (Zimmerman and Yeo, 2000). It reads:

$$l^1 = \frac{r_n^3}{12} + l_0^1 \quad (11)$$

where r_n [m] is the normal separation of the interface, and l_0^1 [m³] is the initial longitudinal hydraulic coefficient, which makes it possible to assign an initial longitudinal transmissivity to the discontinuity even if it is closed from the mechanical point of view. The longitudinal hydraulic coefficient l^1 , defined in Eq. (11), plays the same role in the hydraulic governing equations of the discontinuity as the intrinsic

permeability \mathbf{K} in the hydraulic governing equations of the continuum. Both parameters account only for the geometrical characteristics of the medium through which the liquid flows, i.e., they are independent of the fluid properties. The fluid properties (as well as the time dimension) are introduced via the water dynamic viscosity μ_w in Eqs. (2) and (9), for the continuum and discontinuities, respectively.

The width w will evolve with the normal separation of interface r_n :

$$w = r_n + w_0 \quad (12)$$

where w_0 [m] can be set to be non-zero to assign an initial storage volume to the discontinuity even if it is mechanically closed (Liaudat et al., 2023).

2.3.2. Mechanical problem

The equation of momentum conservation for the interface element reads as follows:

$$\frac{\partial \sigma_c}{\partial l} = \mathbf{0} \quad (13)$$

where l is the longitudinal axis of the interface element, and $\sigma_c = [\sigma_n, \sigma_1]$ [Pa] is the total stress on the interface mid-plane, with σ_n and σ_1 being the normal and shear stress components on that plane. In this paper, mode I fracturing is considered. The shear stress component is therefore not discussed here.

For the mechanical constitutive behaviour of the discontinuity, the bilinear traction–separation law schematically depicted in Fig. 2 is used (Mi et al., 1998; Liaudat et al., 2023). More advanced constitutive laws can be incorporated easily into the code. This bilinear law can describe fracture initiation and propagation characterised by three parameters: the maximum tension strength σ_{n0} [Pa], the normal “cracking” separation r_{n0} [m], and the normal debonding separation r_{nc} . The dashed lines in Fig. 2 represents the unloading–reloading path when reaching the relative displacement r_n^* .

In the loading condition, the normal stresses are given by the following expressions:

$$\sigma_n' = \begin{cases} (1 - D)K_n r_n & \text{if } r_n \geq 0 \\ K_n r_n & \text{if } r_n \leq 0 \end{cases} \quad (14)$$

where σ_n' [Pa] represents Terzaghi's effective normal stress, defined as $\sigma_n' = \sigma_n + p_w^m$, and $K_n = \sigma_{n0}/r_{n0}$ [Pa/m] is the initial normal stiffness. When an interface element is used to represent natural fractures, the stiffness can have a physical meaning, for instance, as a result of interpenetration of fracture surfaces due to presence of asperities (Cerfontaine et al., 2015; Lei and Barton, 2022). In the context of this paper, K_n is interpreted as penalty coefficients, thus allowing negligible interpenetration of fracture surfaces regardless of their roughness (Cerfontaine et al., 2015). To enforce the contact constraints, the stiffness should be set high enough to reduce artificial compliance (Liaudat et al., 2023). However, the stiffness is limited by the Ladyzhenskaya–Babuška–Brezzi condition (Kikuchi, 1982), beyond which the contact stress oscillates due to an ill-conditioned stiffness matrix. Therefore, the choice of their values is a trade-off between having artificial compliance and having numerical convergence problems. Additionally, D is the damage variable ranging from 0 (intact rock) to 1 (fully separated fracture). This damage variable evolves as follows:

$$D = \min \left(\frac{\bar{\omega}}{1 + \bar{\omega}} \frac{1}{\eta}, 1 \right) \quad (15)$$

$$\bar{\omega} = \max(\omega) \quad (16)$$

$$\omega = \left\langle \frac{\langle r_n \rangle}{r_{n0}} - 1 \right\rangle \quad (17)$$

$$\eta = 1 - \frac{r_{n0}}{r_{nc}} \quad (18)$$

where ω is a positive scalar that defines the mechanical degradation of the interface element for a given normal separations (Fabbri et al., 2023), $\langle \cdot \rangle = (\cdot + |\cdot|)/2$ is the Macaulay bracket.

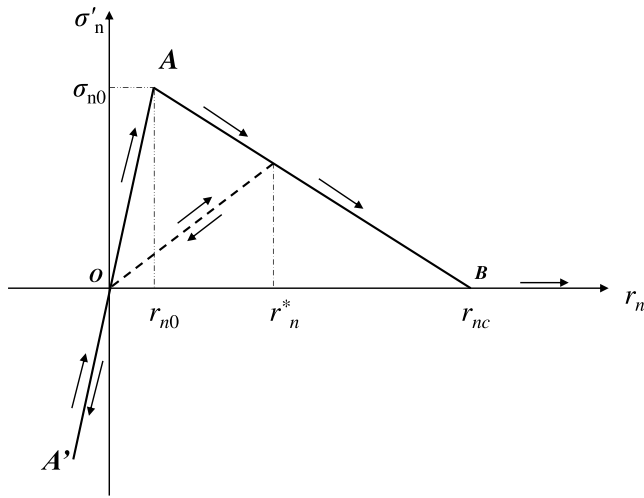


Fig. 2. The elasto-damage law (following Liaudat et al. (2023)). The dashed line indicating the un-loading/re-loading path after reaching relative displacements r_n^* .

2.3.3. Thermal problem

The conservation of energy, in terms of temperature, applied to a differential volume of discontinuity $w dl$ reads:

$$\frac{\partial}{\partial t}(w \rho_w c_{pw} T^m) + \frac{\partial q_T^l}{\partial l} - q_T^b - q_T^t = 0 \quad (19)$$

where q_T^s [J/(m² s)] is the rate of change of the heat stored in the discontinuity, q_T^l [J/(m s)] is the longitudinal heat flow, q_T^b [J/(m² s)] and q_T^t [J/(m² s)] are the normal heat flows incoming from the surrounding continuum medium via bottom and top faces to the discontinuity, respectively.

The terms in Eq. (19) can be expanded as:

$$q_T^l = -w \lambda_w \frac{\partial T^m}{\partial l} + c_{pw} q_w^l T^m \quad (20)$$

$$q_T^b = -\lambda_w \frac{2\check{T}^b}{\max(w, \bar{w})} + c_{pw} q_w^b \check{T}^b \quad (21)$$

$$q_T^t = -\lambda_w \frac{2\check{T}^t}{\max(w, \bar{w})} + c_{pw} q_w^t \check{T}^t \quad (22)$$

where $\check{T}^b = T^m - T^b$ and $\check{T}^t = T^m - T^t$ are the temperature jumps between the bottom or top face and the mid-plane, with T^m , T^b and T^t being the temperatures at the mid-plane, bottom and top face of interface element, respectively, and λ_w is the thermal conductivity of the water. \bar{w} is a penalty coefficient to avoid singularity when interface elements are used to provide potential cracking paths in intact rock. The penalty coefficient should be as small as possible to reduce the artificial compliance.

3. Verification against analytical solutions

Verification is undertaken against analytical benchmarks to verify the reliability of the proposed model in simulating coupled thermo-hydraulic process in the interface element, as well as simulating fracturing processes with hydro-mechanical coupling.

3.1. Thermo-hydraulic coupling in a single fracture

3.1.1. Verification against Lauwerier's problem

The first example considers heat advection along a single fracture combined with heat conduction into the surrounding continuum medium. Lauwerier (1955) and Barends (2010) provided the analytical solution to this problem. In their concept, a homogeneous fracture with a width w is overburdened and under-burdened by two impermeable

rock matrices with a uniform initial temperature T_{ini} , as schematically depicted in Fig. 3(a). Water with a temperature T_{inj} is injected into the fracture at a constant volume rate. The upper and lower faces of the fracture are impermeable to water, but heat conduction into the surrounding matrix is allowed (Barends, 2010). Other assumptions to derive the analytical solution are listed below:

- (1) Temperature across the vertical profile of the fracture is uniform, i.e. no vertical temperature gradient in the fracture.
- (2) Darcy velocity along the fracture is constant.
- (3) Density, specific heat capacity, and thermal conductivity of water are constant.
- (4) Thermal diffusion and dispersion are neglected in the longitudinal direction;
- (5) The domain size is semi-infinite.
- (6) The surrounding matrix are homogeneous and isotropic.

With the above concept and assumptions, the analytical solution for the time evolution of the temperature profile along the fracture is as follows (Lauwerier, 1955; Barends, 2010):

$$T(x, t) = T_{ini} + (T_{inj} - T_{ini}) \operatorname{erfc} \left(\frac{\lambda' x}{\rho_w c_{pw} w \sqrt{\lambda' v_w (v_w t - x) / (\rho' c'_p)}} \right) H \left(t - \frac{x}{v_w} \right) \quad (23)$$

where, T_{ini} and T_{inj} are the initial and injection temperature, respectively, ρ' , λ' and c'_p are the density, the thermal conductivity, and the specific heat capacity of the surrounding matrix, respectively, ρ_w and c_{pw} are the density and specific heat capacity of water, respectively, v_w [m/s] is the Darcy velocity along the fracture, $\operatorname{erfc}()$ is the complementary error function, and $H()$ is the Heaviside function.

To verify the numerical model, the Lauwerier's problem is considered with the parameters indicated in Table 1. The considered numerical boundary conditions are indicated in Fig. 3(a). For simulated times of less than 30,000 s, the domain size of 5×5 m² was found large enough to neglect boundary effects in the heat transport, thus matching the semi-infinite domain assumption of the analytical solution. The interface elements, used to represent the fracture, is placed at the centre of the domain, shown in Fig. 3(b). Fluid flow and heat advection are assumed to be unidirectional along the fracture. The transversal hydraulic coefficients are set to zero to match the assumption of null transversal heat convection. Since the longitudinal heat conduction in the fracture is neglected in the analytical solution, a very low thermal conductivity of 0.001 W/(m K) is adopted for water in the numerical model. The vertical temperature profile in the fracture is assumed to be uniform (i.e. zero vertical temperature gradient) in the analytical solution, therefore, in the numerical model following the approach of Barends (2010) a high thermal conductivity of $\lambda_w = 10$ W/(m K) for transversal heat flow is used in Eqs. (21) and (22). Additionally, the surrounding matrix is set as impermeable, with heat conduction allowed. The initial temperature of the domain is T_{inj} . All input parameters are listed in Table 1. The domain is discretised into 2600 elements, including quadratic continuum elements and interface elements.

The numerical and analytical results are then compared in terms of the temperature profile along the fracture at different times (Fig. 4a) and the temperature evolution at positions $x = 1$ m, 1.5 m, 2 m, and 3 m away from the injection point (Fig. 4b). These plots show an excellent agreement between the numerical and analytical solutions.

3.1.2. Stabilising numerical instabilities for high Péclet number

It is well known that in convection-dominated transport problems, a high ratio between advective and conductive heat transport can lead to numerical instabilities, i.e., oscillations (Pérez Carreras, 2018; Diersch, 2014). Therefore, further consideration and treatment are needed to stabilise the numerical solution. In this section, stabilisation of the

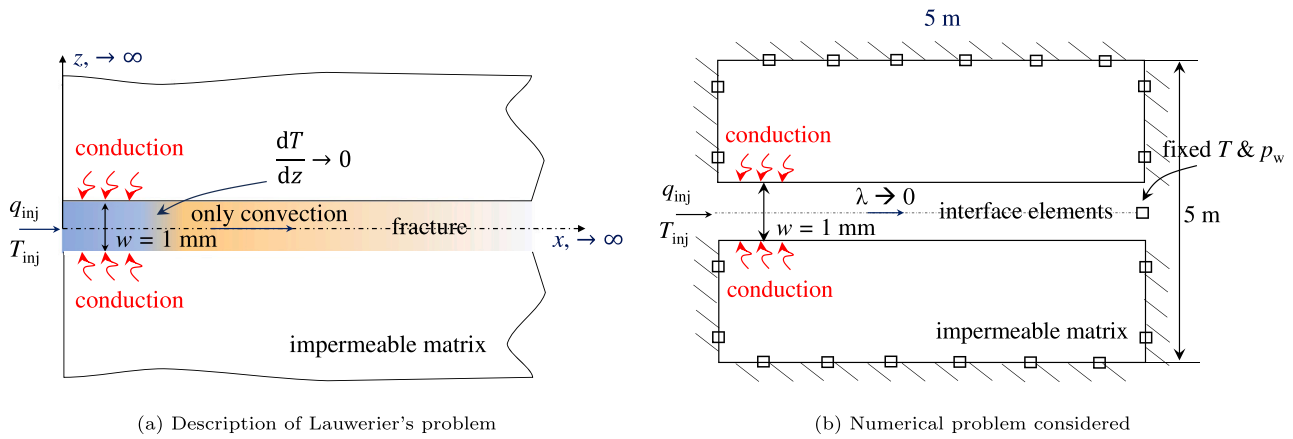


Fig. 3. Description of the problem for analytical and numerical solutions.

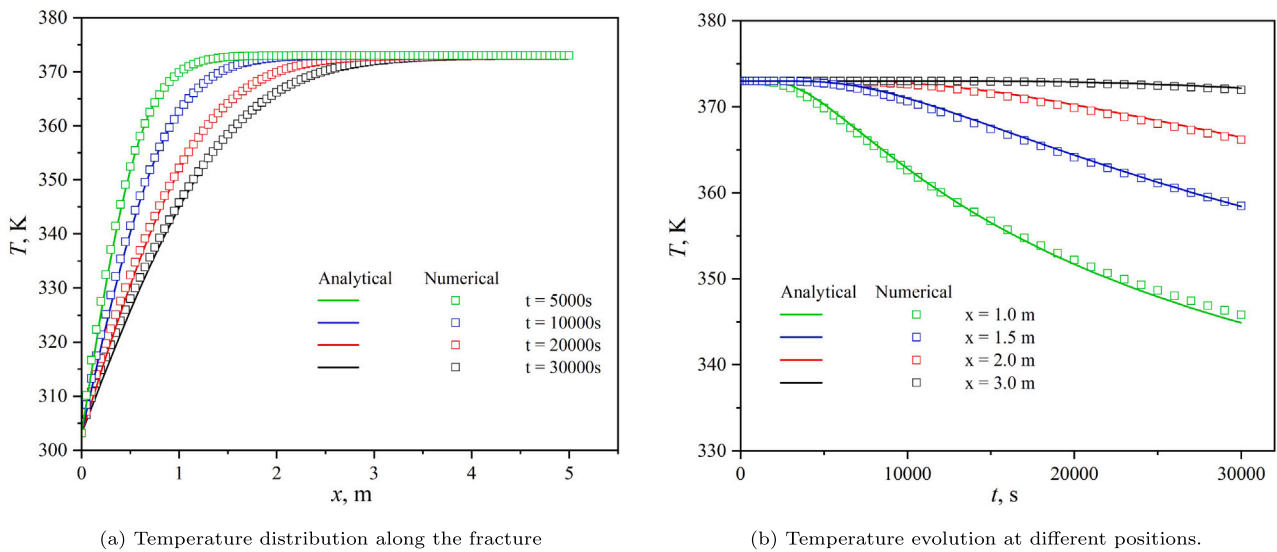


Fig. 4. Comparison of numerical and analytical solutions of Lauwerier's problem.

Table 1
Input parameters for modelling thermo-hydraulic processes in a single fracture.

Parameter	Symbol	Value	Unit
Fracture width	w	0.001	m
Longitudinal hydraulic coefficient	t_0^l	10^{-11}	m^3
Transversal permeability	k_b, k_t	0	m^2
Injection flow rate	q_{inj}	0.00001	m^3/s
Injection temperature	T_{inj}	303	K
Initial temperature	T_{ini}	373	K
Water density	ρ_w	1000	kg/m^3
Water viscosity	μ	0.001	Pa s
Thermal conductivity of water	λ_w	0.001	W/(m K)
Water specific heat capacity	c_{pw}	4184	J/(kg K)
Matrix density	ρ'	2800	kg/m^3
Matrix thermal conductivity	λ'	7.7	W/(m K)
Matrix specific heat capacity	c'_p	850	J/(kg K)

numerical instability is presented, with the results illustrated with the numerical model in Fig. 3(b).

The Péclet number for heat transport in a fracture, Pe , defines the ratio between advective to conductive heat transport:

$$Pe = \frac{\rho_w c_{pw} h v_w^l / w}{2\lambda_w} \quad (24)$$

where w [m] and h [m] are the width and the longitudinal size of the interface element, respectively.

In the numerical solution to the heat transfer problem presented in Fig. 3(b), if the flow velocity is increased or heat conductivity is reduced, numerical instability can be observed and found to be related to Péclet number, as shown in Fig. 5. If no stabilisation method is implemented, oscillations will occur once the Péclet number is greater than 1, and the numerical solution will deteriorate with increasing Péclet number. Multiple methods have been proposed to stabilise the numerical solution, such as upwind Petrov–Galerkin method and Bubble Functions method (Heinrich et al., 1977; Baiocchi et al., 1993). However, introducing the weighting function (as in the Petrov–Galerkin method) or bubble function into the finite element formulation increases computational cost and can be non-trivial. In addition, implementing these approaches in the current code would require significant modifications. A simpler method is to add an artificial diffusion coefficient (λ_a) to the physical diffusion coefficient (λ_w), called the Balance Equation Method (Owen, 1984; Pérez Carreras, 2018). The artificial diffusion coefficient is defined as:

$$\lambda_a = \delta \rho_w c_{pw} h |v_w^l| / w \quad (25)$$

where δ is a tuning parameter. To stabilise the solution, the Péclet number must always be smaller than 1, therefore a tuning parameter equal to around 0.5 ensures stability. The Péclet number after stabilisation is

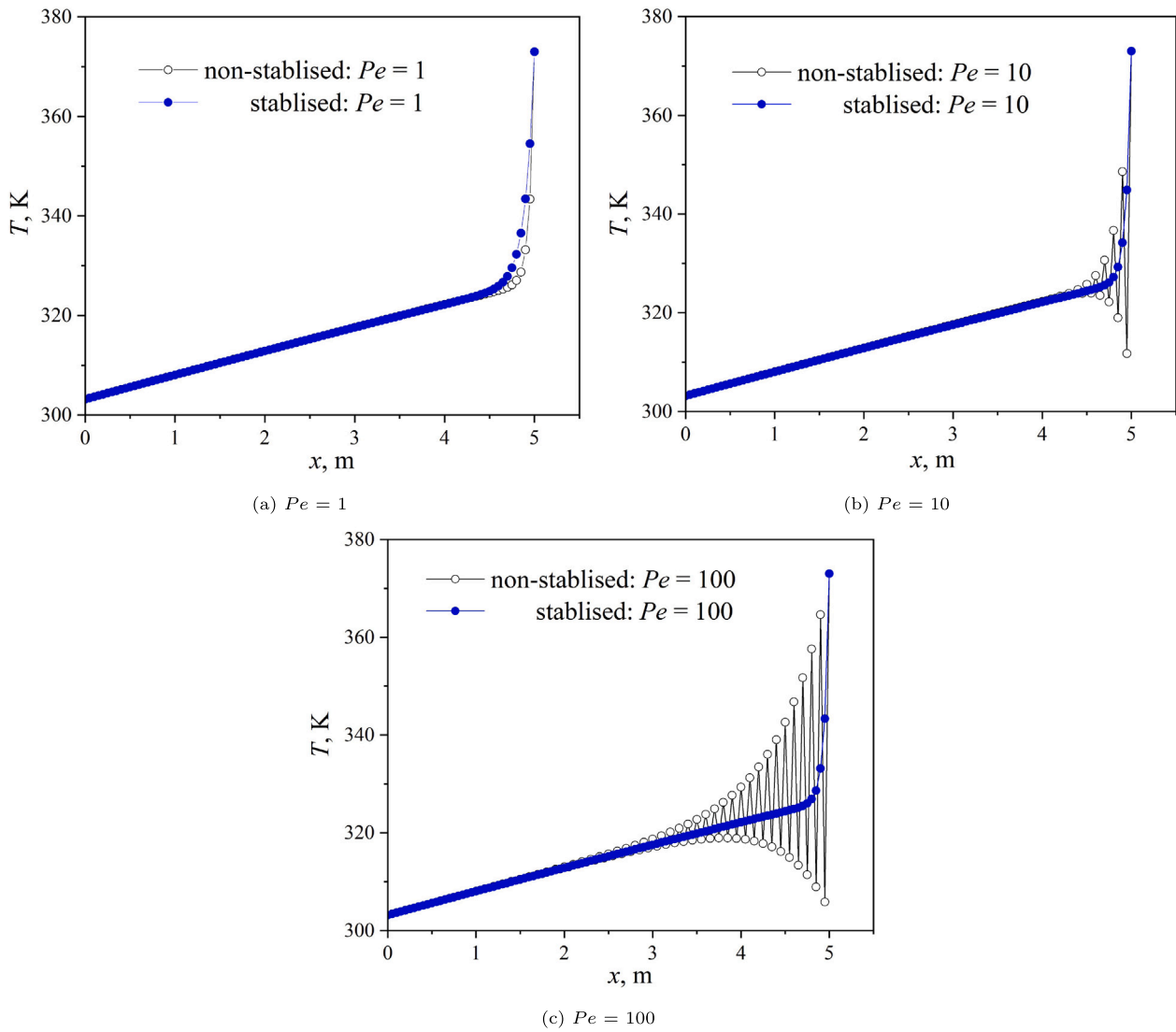


Fig. 5. Temperature profile along the fracture at time step 5000 s, with and without stabilisation. A tinning parameter of 0.5 is used to stabilise the numerical solution due to high Péclet number in longitudinal heat flow in a fracture.

then:

$$Pe = \frac{\rho_w c_{pw} h v_w^l / w}{2(\lambda_w + \lambda_a)} \quad (26)$$

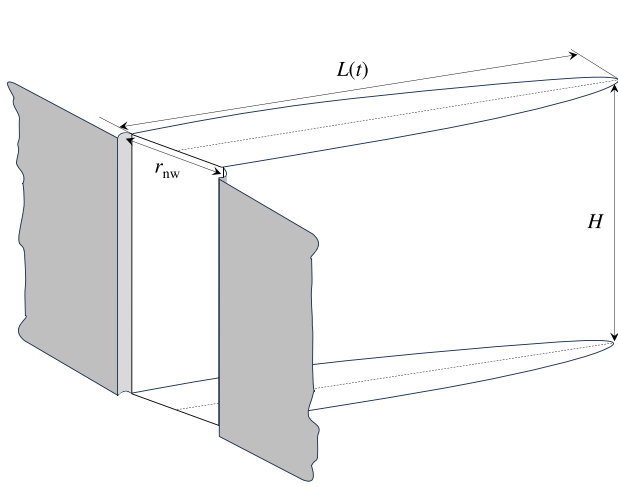
This method is only valid for cases without internal energy sources (or sinks), i.e., the right-hand side of Eq. (19) is 0. Because in our research, generally no internal energy sources/sinks exist, the balance equation method is implemented here to stabilise the solution. Temperature profile along the fracture under different Péclet number is shown in Fig. 5. The stabilised solution shows no oscillation even when the original Péclet number is 100, and meanwhile shows good agreement with non-stabilised solution when Péclet number is 1. It should be noted that, as is shown in Fig. 5(a), the added artificial diffusion can result in slight deviation from the exact solution, due to the added conduction to achieve stabilisation. Yet, conduction accounts for only small part of the heat transfer along the fracture and conduction in the matrix is more important. Consequently, the results remain accepted accuracy.

3.2. Hydro-mechanical processes - KGD model

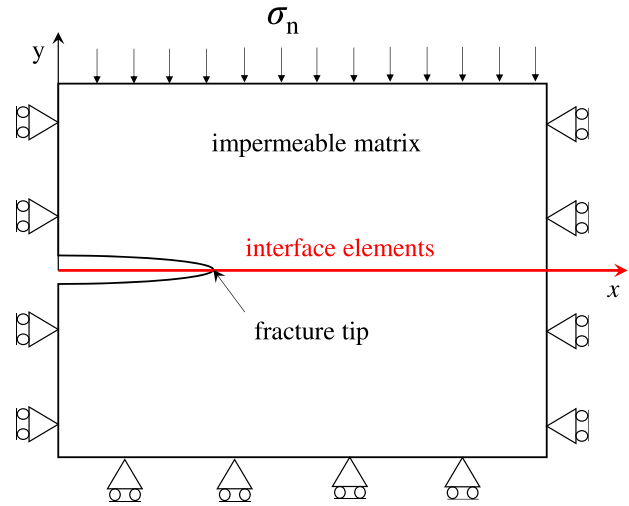
In this example, fracture propagation as a result of localised water injection in an infinite, homogeneous and impermeable medium without leak-off is considered under plane-strain conditions. The KGD

model (Fig. 6(a)), proposed by Khristianovic and Zheltov (1955) and Geertsma and De Klerk (1969) has been widely used to verify numerical solutions to hydraulic fracturing, and is used here to provide analytical solution to the considered problem. The KGD model assumes a fracture with a rectangular shape in the vertical plane with an elliptical shape in the horizontal plane, as is shown in Fig. 6(a). The rectangular vertical cross section extends from the injection face with the maximum aperture to the fracture tip with a null width (Geertsma and De Klerk, 1969). Initially, the fracture is assumed to be without any appreciable opening. At $t_0 = 0$ s, water with a constant volumetric injection rate Q_0 is injected. The injected fluid flows through the fracture without leak-off into the surrounding medium. The fracture opens and propagates as the fluid pressure diffuses along the fracture. Other assumptions of the KGD model are Valkó and Economides (1995), Spence and Sharp (1985) and Adachi and Detournay (2002):

- (1) The rock matrix is linear elastic.
- (2) The fracture has a constant height in the vertical direction.
- (3) The fracture aperture at the fracture tip is zero.
- (4) Zero-toughness condition is assumed, i.e., no mechanical energy spent on fracture propagation;
- (5) Zero-lag condition is assumed, i.e., no lag between fluid and the fracture tip;



(a) KGD geometry in 3D view, modified from Valkó and Economides (1995)



(b) Numerical model

Fig. 6. Description of KGD model.

- (6) The flow rate along the fracture is everywhere equal to the injection.
 (7) Fluid flow is solved based on lubrication theory.

With the above basic assumptions, Adachi and Detournay (2002) have proposed the following analytical solutions to obtain the evolution of the half length of the fracture L , the aperture at the fracture mouth (at the injection point) r_{nw} , and the net pressure at the fracture mouth $p_{n,w}$:

$$L(t) = 0.466 \left(\frac{E' Q_0^3}{\mu} \right)^{1/6} t^{1/3} \quad (27)$$

$$r_{nw}(t) = 0.924 \left(\frac{\mu Q_0^3}{E'} \right)^{1/6} t^{1/3} \quad (28)$$

$$p_{n,w}(t) = 2.28(E'^2 \mu)^{1/3} t^{-1/3} \quad (29)$$

where $E' = \frac{E}{1-\nu^2}$ [Pa] is the plane strain modulus, with E [Pa] and ν being the Young's modulus and the Poisson's ratio of the rock matrix, Q_0 [m^3/s] is the constant volumetric injection rate, and μ [Pa s] is the fluid viscosity.

To numerically solve the viscosity-dominated KGD problem, a $5 \times 10 \text{ m}^2$ ($X \times Y$, X is the size in the direction of fracture propagation while Y the size in the direction perpendicular to fracture propagation) domain with interface elements inserted at the middle is considered, shown in Fig. 6(b). The domain size is chosen so that the conditions $Y \geq 10L(t_f)$ and $X \geq 2L(t_f)$, where t_f is duration of the water injection, are met. This condition was proved sufficient to avoid effects from boundary conditions (Settgast, 2022). Considering only half-wing of the KGD fracture is modelled, the injection rate in the simulation is $Q_0 \rho_w / 2$. To simulate the viscosity dominated condition, the fluid viscosity is set to 1 mPa s, while the tensile strength is set to 1000 Pa (Settgast, 2022). Other parameters are presented in Table 2.

The simulation results are compared with the analytical solution in Figs. 7(a) to 7(c). A good general agreement between the numerical and analytical solutions is appreciated. The initial increase phase of the simulated $p_{n,w}$ at the beginning of injection observed in Fig. 7(a) is because in the model the flow rate is linearly increased from 0 to $Q_0 \rho_w / 2$ in a very short time (0.1 s). In addition, the deviation observed in all comparisons can be explained as a result of the assumed fracture shape in the analytical solution and the ability of the numerical solution to respond to the mechanical perturbation. As stated earlier, the analytical solution assumes an elliptical shape along the fracture

Table 2
Material parameters for KGD numerical model.

Parameters	Symbols	Values	Units
Young's modulus	E	20	GPa
Poisson's ratio	ν	0.20	–
Tensile strength	σ_{n0}	1000	Pa
Cracking separation	r_{n0}	1×10^{-12}	m
Debonding separation	r_{nc}	1^{-10}	m
Fluid density	ρ_w	1000	kg/m^3
Fluid viscosity	μ	0.001	Pa s
Injection rate	$Q_0 \rho_w / 2$	5×10^{-4}	kg/s

($r_n = r_{nw} \sqrt{1 - \frac{x}{L(t)}}$, Garolera Vinent, 2017). However, the numerical model does not give exactly the same shape, due to the intrinsically imposed geometric restriction at the fracture tip ($\frac{dr_n}{dx} = 0$), which results in a sigmoid close to the tip (Fig. 7(d)) (Garolera Vinent, 2017).

4. Validation

To validate the numerical model, simulations of the thermal fracturing experiments conducted by Zhang et al. (2019) are carried out. A brief recap of the experimental procedure is given below, followed by the introduction to the numerical model and the comparison of simulation and experiment results. Finally, a sensitivity analysis is performed to show how the key parameters can influence the model performance. A 2D approach to the modelling is taken in order to reduce the computational load. This is considered to be sufficient to simulate the general processes and especially as in 3D material heterogeneities will play a further role in the specific fracture evolution. The evaluation of the performance will focus general on the qualitative behaviour, with a lower focus on the quantitative performance.

4.1. Recap of the experiment

The aim of the experiments conducted by Zhang et al. (2019) was to study the influence of cold water injection on the hydraulic fracturing processes. Granite samples (properties listed in Table 3) with dimensions of $0.1 \text{ m} \times 0.1 \text{ m} \times 0.12 \text{ m}$ were used. A hole was drilled in each sample, and a pipe with perforated holes was placed into the drilled hole with the dimensions shown in Fig. 8. The annulus between the wellbore and the wall of the drilled hole was sealed.

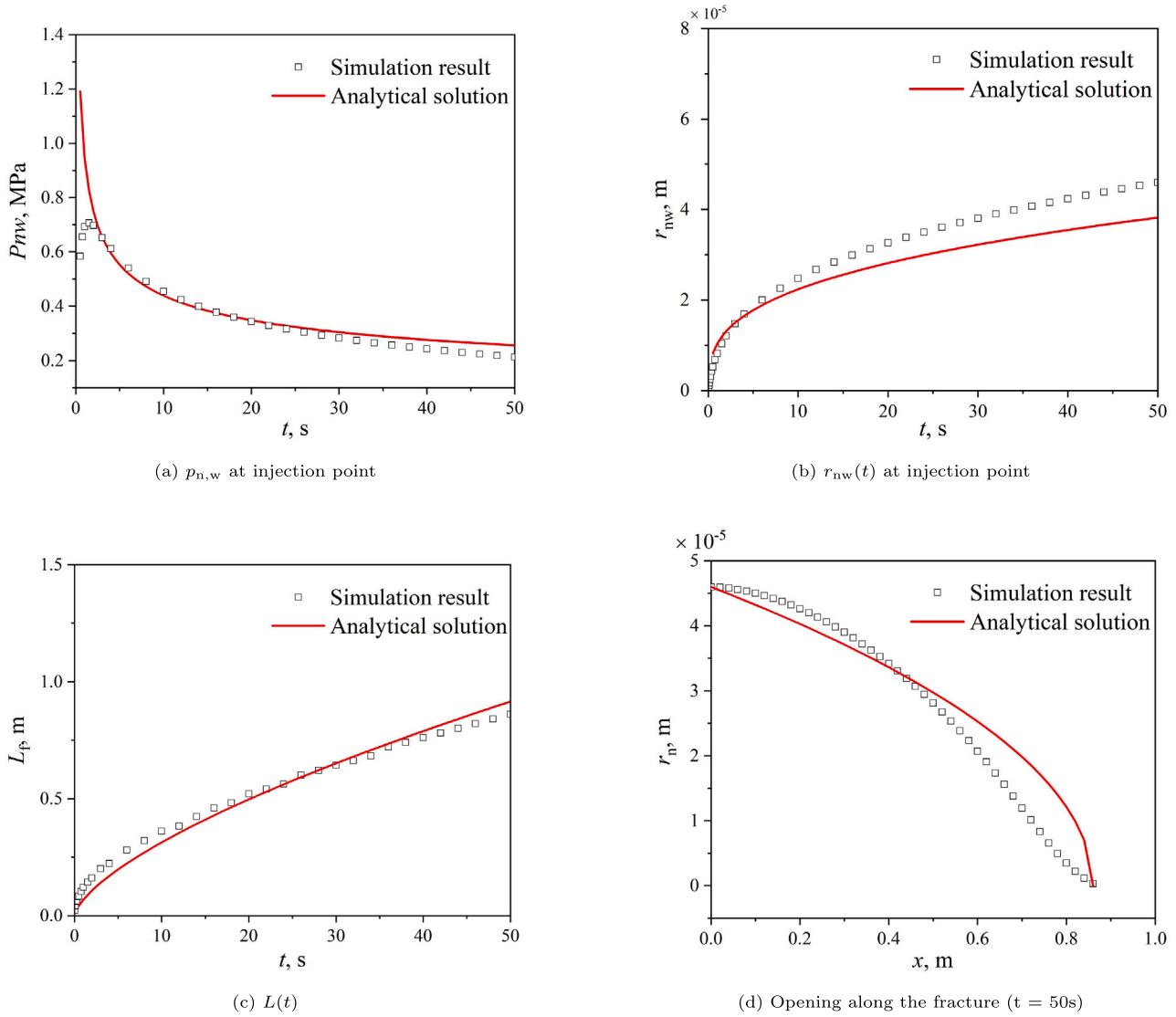


Fig. 7. Comparison of simulation results and analytical solutions of the KGD problem.

Table 3

Properties of granite samples used in the experiment, data from Zhang et al. (2019).

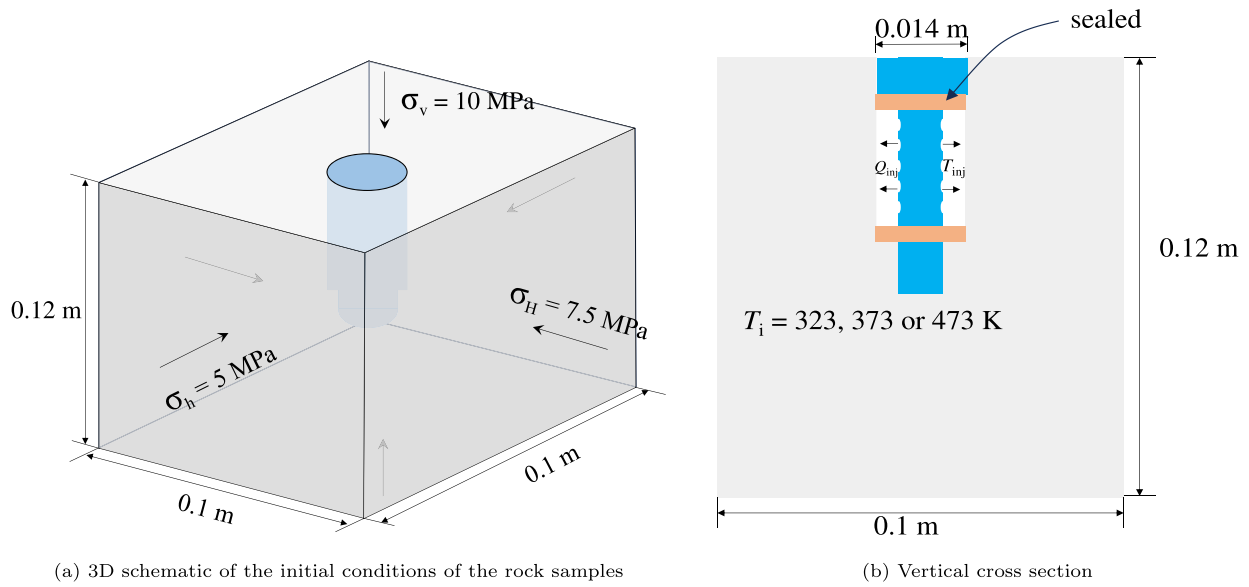
Parameter	Symbol	Value	Unit
Porosity	ϕ	0.14	–
Permeability	K	6×10^{-19}	m^2
Young's modulus	E	32	GPa
Poisson's ratio	ν	0.2	–
Tensile strength	σ_t	20.5	MPa
Density	ρ_s	2590	kg/m^3
Volumetric thermal expansion coefficient	β_s	6.2×10^{-6}	$1/K$
Specific heat capacity	c_{ps}	950	$J/(kg^{-1} K^{-1})$
Thermal conductivity	λ_s	4	$W/(m^{-1} K^{-1})$

The samples were then slowly heated to 323 K, 373 K and 473 K with the temperature maintained for 12 h to ensure uniform and complete heating. Subsequently, an anisotropic stress was applied to the samples, with $\sigma_v = 10$ MPa, $\sigma_H = 7.5$ MPa and $\sigma_h = 5$ MPa (Fig. 8(a)). Distilled water with a temperature of 293 K was injected into the wellbore under controlled-rate condition to induce fractures. In the description of the experiments (Zhang et al., 2019), the controlled-rate condition was not presented. However, it can be back-calculated from the water pressure response curve, as it is discussed below.

The injection pressure response was monitored and presented in Fig. 9. After the fracturing experiment, red ink was injected to visualise the fractures. The results show red ink diffused in the direction perpendicular to the minimum in-situ stress when the rock temperature was 373 K, indicating a single fracture formed in that direction (Fig. 11a). In contrast, red ink diffused in all directions when the rock temperature was 473 K, indicating fracture branching (Fig. 11b).

4.2. Numerical model

A 2D symmetric numerical model with a size of $0.1 \times 0.05 m^2$ (upper half domain) is built to simulate the experiments (Fig. 8(c)). A horizontal plane strain condition is chosen because the maximum stress is σ_v , which means vertical fractures are expected to be induced (and were observed in the experiments) (Zhang et al., 2019). A hole with a radius of 0.007 m is placed at the centre. The boundary conditions are shown in Fig. 8(c). Initial stresses σ_H and σ_h are set for the elements. Due to symmetry, only half of the domain is considered. Two models were considered to represent possible fractures. Firstly, Model A, which had a single line of interface elements in the direction of maximum horizontal stress, was used to validate against the experimental results with rock temperature of 323 K and 373 K. In these two cases, only a single main fracture was observed so that a pre-defined cracking path in

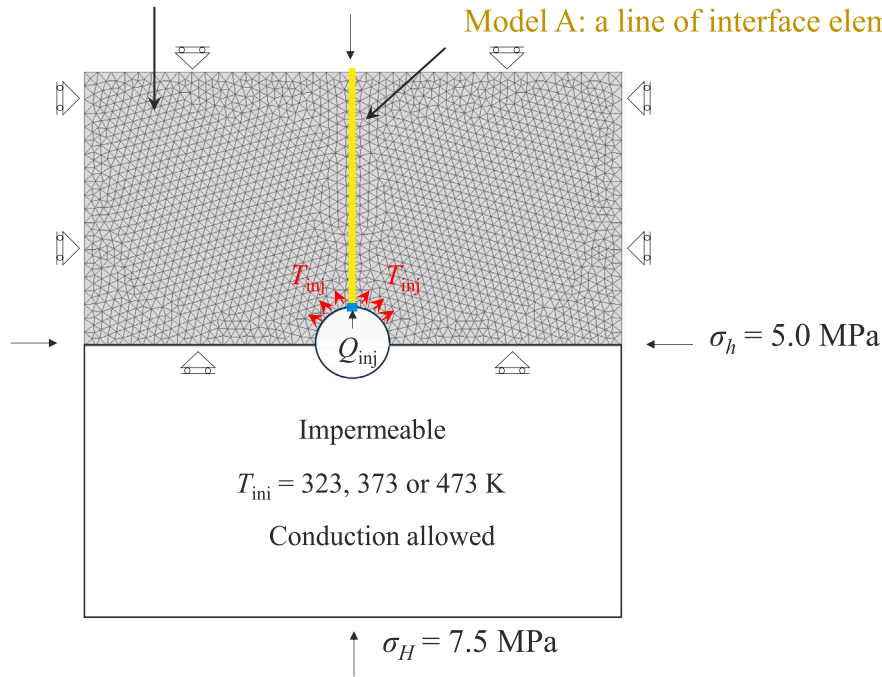


(a) 3D schematic of the initial conditions of the rock samples

(b) Vertical cross section

Model B: interface elements between all continuum elements

Model A: a line of interface elements



(c) Horizontal cross section (numerical model)

Fig. 8. Schematic description of the experiment (modified from Zhang et al. (2019)) and simulation.

the model is possible. Secondly, Model B, which had interface elements in between all continuum elements, was used to investigate fracture branching, as was observed when the rock was heated to 473 K.

As the permeability of the intact rock is extremely low ($6 \times 10^{-19} \text{ m}^2$), the continuum elements that represent the intact rock are set to be impermeable, while thermal conduction is allowed. This is done by setting k^b and k^t to zero. Injection rate is imposed only at the mouth of the interface element that is at the wellbore in the direction of the maximum horizontal stress, while the temperature boundary condition is imposed around the wellbore. To simulate the behaviour of the intact rock yet allowing only fluid flow in the interface elements, we set the initial aperture and hydraulic coefficient of interface elements to give behaviour equivalent to the rock sample, based on the rock sample's

porosity and permeability, given by the following equations:

$$t_0^l = kL^* \quad (30)$$

$$w_0^l = \phi L^* \quad (31)$$

where $k[\text{m}^2]$ and ϕ are the rock permeability and porosity, respectively, $L^*[\text{m}]$ is the characteristic element length, defined as the dominant size of the continuum elements in the mesh, which can be obtained via mesh quality analysis. For this study $L^* = 0.00163 \text{ m}$.

In the simulation, the injection rate is fixed at the mid-plane node of the first interface element at the borehole in the direction of the maximum stress, indicated by the blue rectangle in Fig. 8(c). Since the injection rate was not disclosed in the original paper (Zhang et al., 2019), it is back-calculated from the experimental pressure response

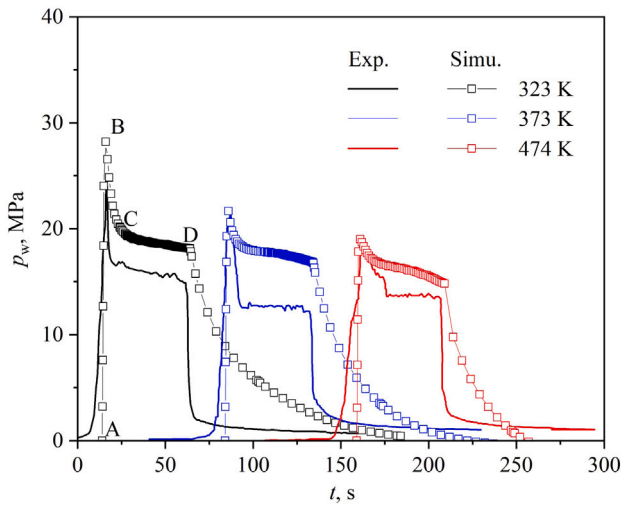


Fig. 9. Comparison of pressure response curves from simulations (Model A) and experiments by Zhang et al. (2019).

Table 4

Input parameters for the simulation, data partly from Zhang et al. (2019).

Parameter	Symbol	Value	Unit
Rock temperature	T_i	323, 373, or 473	K
Injection temperature	T_{inj}	293	K
Injection rate	q_{inj}	3×10^{-6}	kg/(m s)
Water density	ρ_w	1000	kg/m ³
Water viscosity	μ	0.001	Pa s
Water specific heat capacity	c_{pw}	4184	J/(kg ⁻¹ K ⁻¹)
Water thermal conductivity	λ_w	0.598	W/(m ⁻¹ K ⁻¹)
Initial hydraulic conductivity	k'_0	1E-21	m ³
Initial aperture	w_0	2E-4	m
Tensile strength	σ_t	20.5	MPa
Cracking separation	r_{n0}	3×10^{-8}	m
Debonding separation	r_n^*	2×10^{-6}	m

curve by running a model without interface to reach the breakdown pressure and selecting the corresponding injection rate. Note that the injection rate q_{inj} here is 2D, and can be approximately linked to 3D by multiplying the height of the open-hole section, through which the fluid was injected. Since the highest Péclet number reached in this exercise is around 0.017, stabilisation technique is not needed. Therefore the tuning parameter λ_a in Eq. (25) is 0 in this case. Except for rock properties listed in Table 3, other input parameters of the simulation are presented in Table 4. The simulation results are then compared to experimental pressure curve to show the agreement between the simulation and experiments under each temperature setting, i.e., 323 K, 373 K and 473 K. After that, a sensitivity analysis on injection rate (q_{inj} , kg/(m s)), tensile strength (σ_t) and debonding separation (r_n^*) is performed.

4.3. Comparison between simulation and experimental results

The pressure response curves (offset in time for visualisation) from Model A and experiments are compared in Fig. 9. The pressure is monitored at the mouth (the blue rectangle shown in Fig. 8(c), mid-plane node) of the line of the interface elements, at which the fluid was injected with a fixed flow rate. It is shown in Fig. 9 that Model A successfully simulates the pressure response during the whole fracturing processes. Both experimental and numerical results show after a linear pressure increase (Stage A–B in Fig. 9), a peak stress at point B, followed by a non-linear pressure drop (Stage B–C) that corresponds to unstable fracture propagation stage and a nearly constant pressure response (Stage C–D) that corresponds to a stable fracture propagation

stage. After injection stops at Point D, pressure drops to zero both in the experiment and numerical simulation, yet at a different rate.

A decrease in peak pressure (the pressure that is required to fracture the rock) with increasing rock temperature is observed both in simulation and experiment consistently. This is because a greater reduction in confining stress due to stronger cooling effect makes fracturing more likely. Fig. 10 illustrates the simulated evolution of fracture aperture in Model A. It shows that with increasing initial rock temperature, i.e. stronger cooling shock, the fracture aperture is significantly larger. In addition, fracture closing can be observed in Fig. 10 at $t=90$ s, which occurs after the injection stops, i.e., after point D in Fig. 9.

Fig. 9 illustrates that in the initial linear pressure response (Stage A–B), the numerical solution shows a more steep curve compared to that of the experimental result. This can be attributed to the fact that the fluid used in the experiment was not de-aired and thus had a higher compressibility, as well as to the storage effect of the experimental equipment. In addition, the simulated fracture propagation pressures (i.e., the nearly constant pressure response in Fig. 9) are higher than those from experiment for all three cases. This could be because the model assumes a fixed-displacement in X direction at both left and right boundary (see Fig. 8(c)), which constrains the opening of the fracture. Moreover, the gradual decrease after point D in the simulated injection pressure is a result of boundary conditions (fixed zero flow rate at injection point while fixed pressure at the ending point of the interface elements after injection stops). The details of the pressure in the injection system after injection was stopped is not presented, so this is likely to be due to differences in the boundary conditions in the experiment and the numerical model.

Fig. 12 compares the first principal stresses in Model A with different initial rock temperatures. High tensile stresses of up to 68 MPa, much higher than rock tensile strength, are observed around the wellbore when initial rock temperature is 473 K. This indicates tensile failures should occur not only in the initial direction of maximum stress, but also around the wellbore when initial rock temperature is 473 K. In contrast, when initial rock temperature is 373 K or 323 K, the stress around the borehole remains lower than rock tensile strength, indicating no tensile failures occur except in the direction of the maximum stress. This is consistent with the experimental results (Fig. 11), which show that the red ink diffused in all direction when rock temperature was 473 K, indicating fracture branching, while only diffused in the direction of maximum in-situ stress at 373 K, indicating a single fracture in that direction. This is to say, our model with interface elements inserted in the direction of maximum stress can qualitatively match the experimental results for the cases with initial rock temperatures of 323 K and 373 K, but it is not able to capture the fracture branching observed when initial rock temperature is 473 K.

To show the capability of the proposed model to simulate fracture branching, interface elements are inserted in between all the continuum elements in Model B to provide potential cracking paths in other directions, at the expense of increasing the computational cost. Fig. 13 shows the simulated fracture opening with the first principal stress plotted from Model B. It can be clearly seen fractures are also induced in other directions except for the direction of the maximum stress when the rock temperature is 473 K. In contrast, only a single fracture is formed when the rock temperature is 323 K or 373 K, though fracturing is allowed to happen in other directions. This shows a good agreement with the experimental results.

This validation exercise further demonstrates the advantage of using the triple-node scheme, rather than double-node one, for interface elements. In double-node elements, the mid-plane water pressure, which is used to compute the longitudinal flux and is considered for H–M coupling, is obtained as the average of the pressures on both sides of the interface. Accordingly, an increase of fluid pressure at the mid-plane can only occur at the expense of increasing the water pressure at the side nodes, which are shared with the surrounding continuum elements. However, any increase in water pressure at these nodes

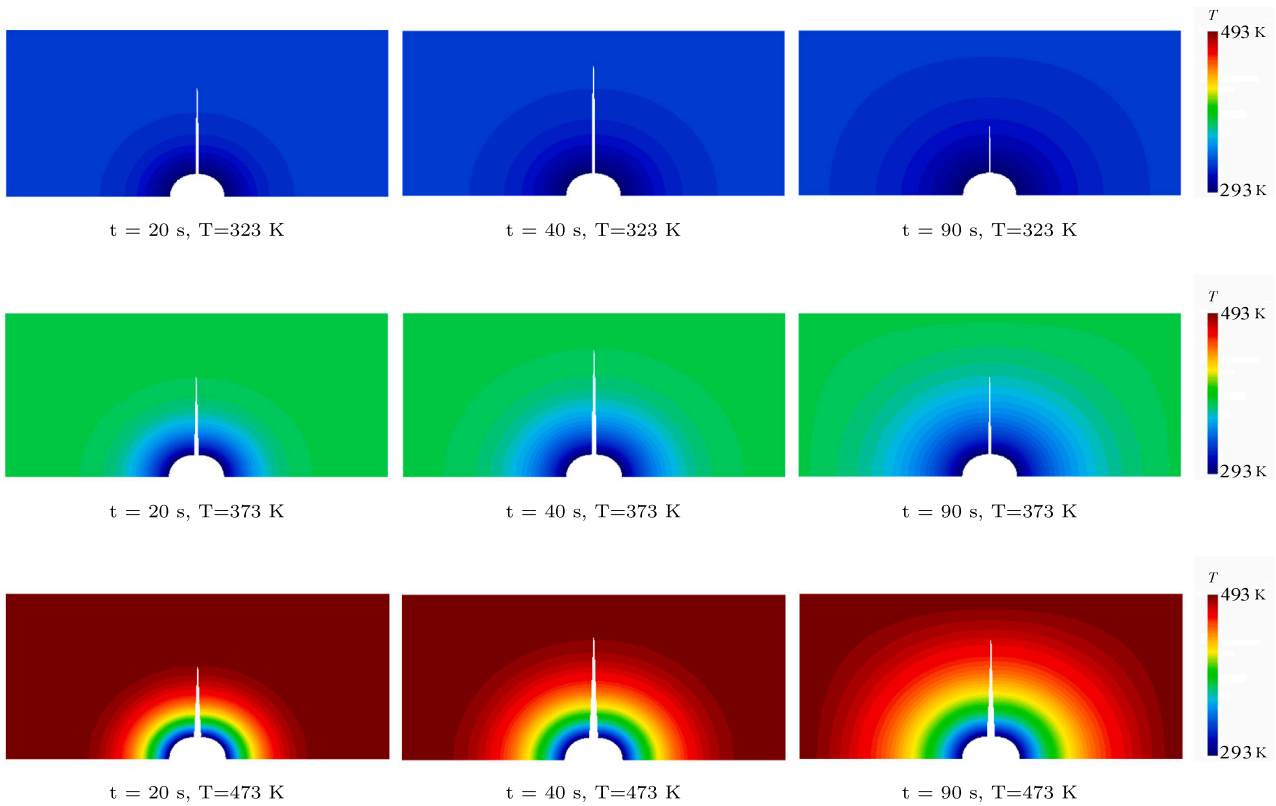


Fig. 10. Fracture aperture evolution under different in-situ temperatures (fracture opening is scaled up 300 times). For all cases, the injection starts at 0 s and ends at 50 s, while the simulation ends at 168 s.

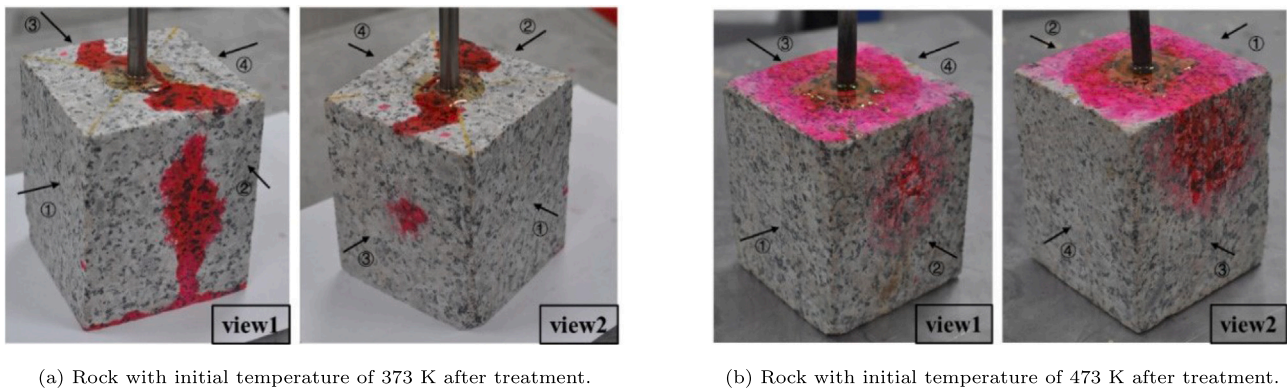


Fig. 11. Experimental results from Zhang et al. (2019) showing red ink diffusion in rock with an initial temperature of 373 K and 474 K.¹

automatically raises the water pressure at the integration points of the surrounding continuum elements through the interpolation functions. This occurs even if the continuum medium is considered impervious and the transversal hydraulic coefficient of the interface is set to zero, leading to numerical convergence issues when water cannot be transferred from the interface elements into the pores of the surrounding continuum. Moreover, these issues depends on the size of the surrounding continuum elements, introducing another source of mesh dependency. In contrast, in triple-node elements, the mid-plane pressure is evaluated independently of the side pressure. By setting k^b and k^l to zero, the mid-plane nodes become completely independent of the side nodes for the hydraulic problem. Consequently, an increase in water pressure at the mid-plane nodes (i.e., inside the fracture) does not change the amount of water stored in the continuum. Note, however, that for the mechanical problem, the effect of the fluid pressure inside the fracture is maintained, as the H-M coupling is established through the mid-plane pressure.

4.4. Sensitivity analysis

Sensitivity analysis is performed on the injection rate (q_{inj}), longitudinal hydraulic conductivity t'_0 and specific fracture energy in Mode I ($G_{IC} = \frac{1}{2}\sigma_{n0} \cdot r_{nc}$) for both Model A and Model B, respectively. When performed against varying G_{IC} , σ_{n0} is fixed while r_{nc} is changed, and vice versa.

Results in Figs. 14(a) and 15(a) show that, as expected, for both models, higher injection rate leads to a higher pressure response, including the peak pressure and propagation pressure (which is not necessarily stable). This injection rate dependency of the pressure response is consistent with other laboratory experiments and numerical

¹ Reprinted from Zhang et al. (2019) with permission from Elsevier. License No.: 5764200568636.

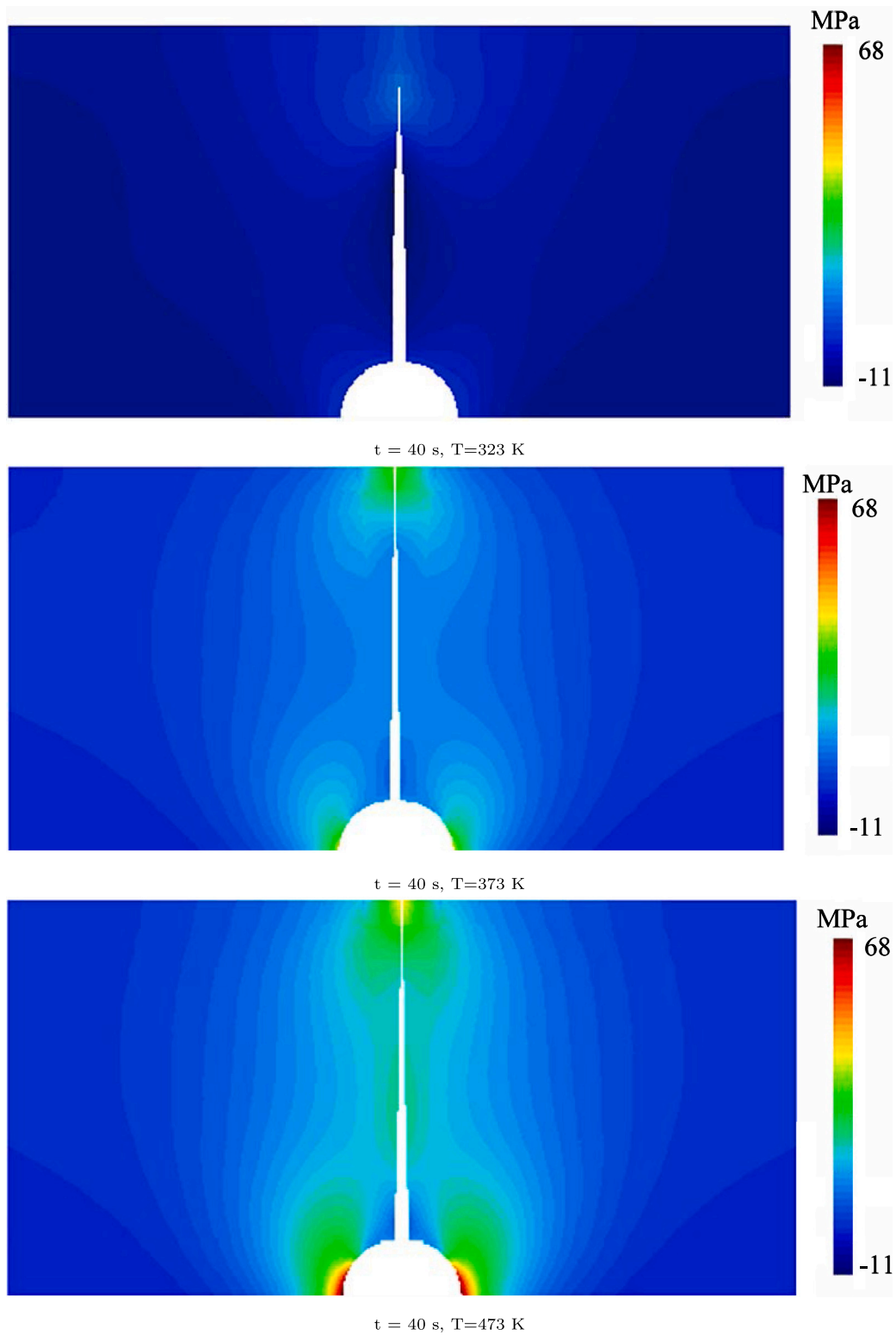


Fig. 12. First principal stress field (σ_1) for different initial temperatures in Model A. When the temperature is initially 473 K, tensile stress significantly greater than the tensile strength (20.5 MPa) is observed at the wellbore (fracture opening is scaled up 1000 times).

simulations in the literature (Zhuang et al., 2019; Cheng et al., 2021; Fallahzadeh et al., 2017), and it is well accepted by engineers (Guo et al., 1993). In addition, higher specific fracture energy (both fixed σ_{n0} and fixed r_{nc}) leads to higher pressure response for both models, due to the increasing resistance. But the peak pressure in the pressure

response curve shows less sensitivity to the case with σ_{n0} fixed in Figs. 14(b) and 15(b), compared to Figs. 14(c) and 15(c). As for the hydraulic conductivity, an increase in t'_0 leads to an increase in the pressure response for Model A, while for model B only an increase in the breakdown pressure is significant.

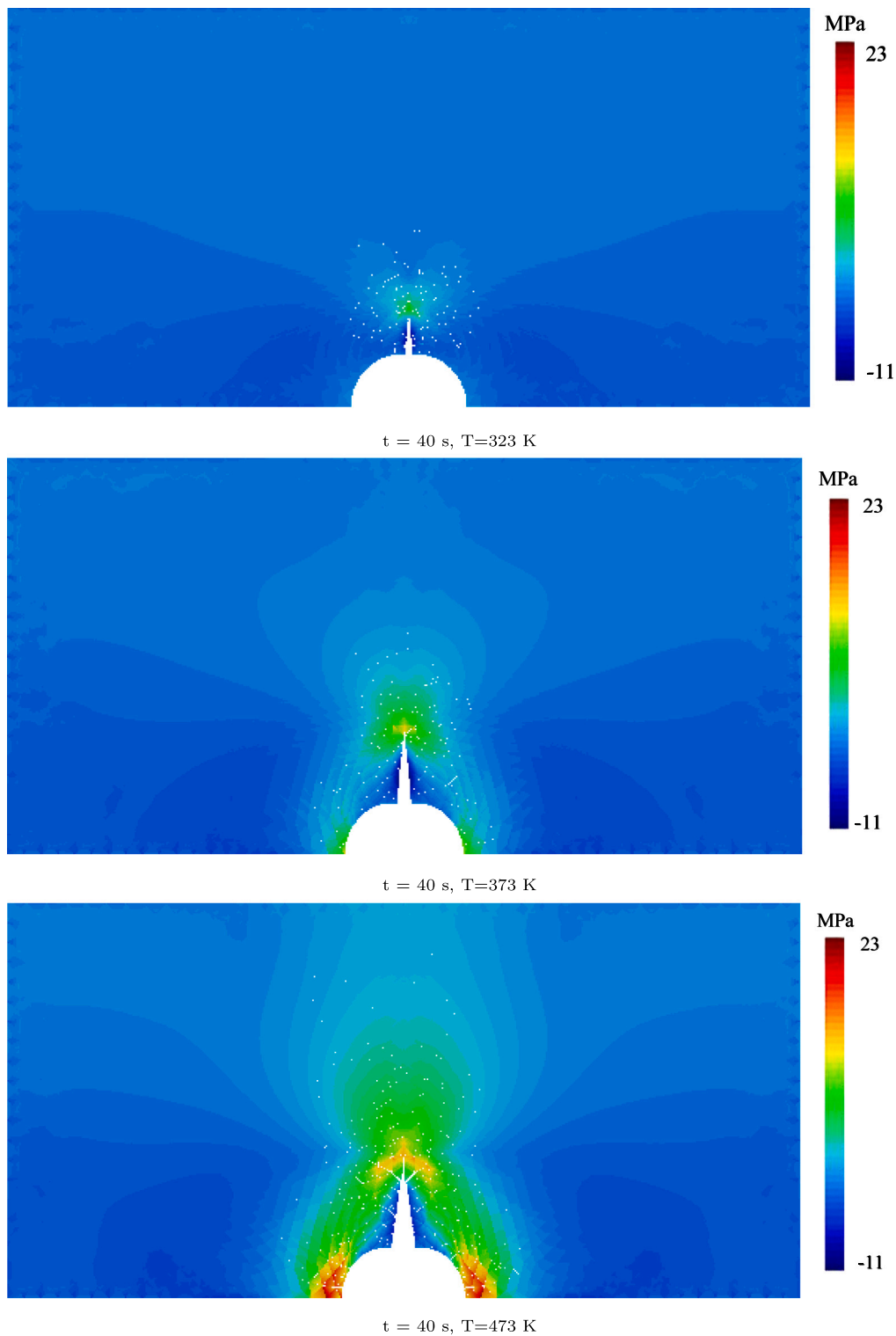


Fig. 13. First principal stress field σ_1 under different initial temperatures in Model B. When temperature was initially 473 K, induced fractures are also observed in other directions, while for other two cases, only a single fracture is induced as it is in the model with only a single line of interface elements inserted in the direction of σ_{yy} . (Fracture opening is scaled up 1000 times).

5. Conclusion

In this paper, a method is developed to simulate fracturing processes under geothermal conditions using the cohesive zone model considering fully THM couplings. Possible discontinuities are represented by zero-thickness triple-noded interface elements, which allow solid elements to separate with mechanical damage and the simulation of

longitudinal and transversal fluid/heat flow in the discontinuity. The cubic law is used to update the fracture transmissivity as a function of its aperture, while an elasto-damage law to characterise the mechanical response of the discontinuity. To simulate pre-existing fractures or fracture initiation/propagation in an intact rock, interface elements can be inserted in between continuum elements surrounding pre-existing

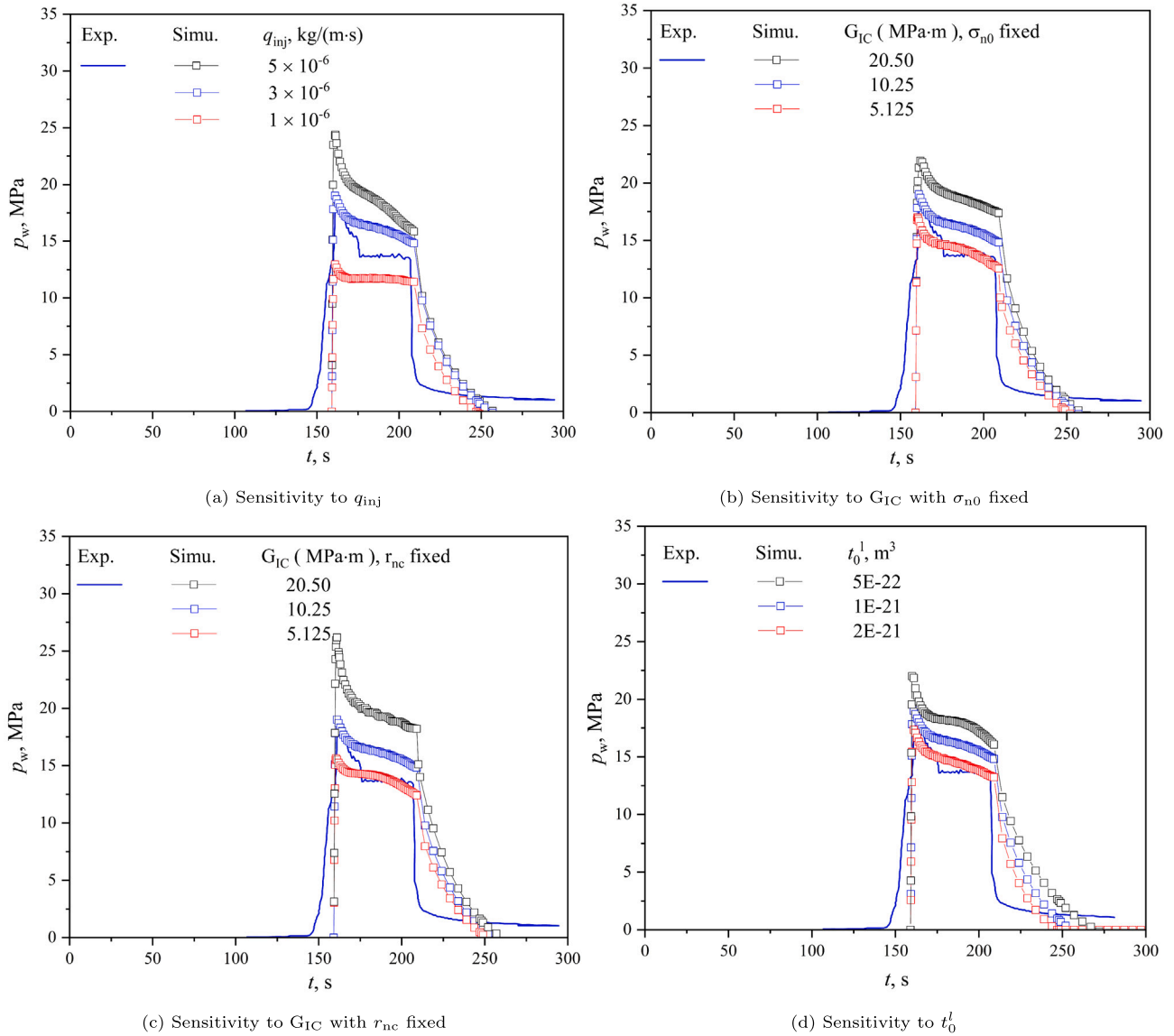


Fig. 14. Sensitivity analysis Model A: the influence of injection rate Q_{inj} , specific fracture energy G_{IC} and the initial longitudinal hydraulic conductivity t_0^l on pressure response.

fractures or in between all continuum elements to provide potential crack paths, respectively.

The method is verified against analytical benchmarks and validated against experimental data on cold water injection into rock samples. The verification shows that the numerical solutions match well with the analytical solutions, illustrating the correctness of the numerical scheme. The validation shows a good agreement between the numerical and experimental results, demonstrating that the model is able to simulate THM processes and, in particular, cracking around a wellbore impacting the inflow ability during and after cold water injection. The proposed method has several potential applications beyond geothermal reservoirs. It can be used to optimise oil and gas recovery via hydraulic fracturing and soft stimulation techniques, such as thermal stimulation and cyclic stimulation, where the opening of the fractures leads to strong thermo-mechanical and hydro-mechanical couplings. In addition, its flexible representation of transversal fluid and heat flows allows simulation of the interface between permeable and impermeable materials (e.g., artificial fractures in enhanced geothermal systems or steel casing-cement interface), existing discontinuities with filling material, or fractures where the pore space at both sides is progressively clogged by chemical or mechanical processes.

CRedit authorship contribution statement

Wen Luo: Writing – review & editing, Writing – original draft, Validation, Software, Methodology, Formal analysis, Data curation, Conceptualization. **Joaquín Liaudat:** Writing – review & editing, Software, Methodology. **Josselin Ouf:** Writing – review & editing, Formal analysis. **Anne-Catherine Dieudonné:** Conceptualisation, Methodology & Writing – review & editing, Supervision, Software. **Florian Amann:** Writing – review & editing, Supervision, Funding acquisition. **Philip J. Vardon:** Conceptualisation, Writing – review & editing, Supervision, Project administration, Funding acquisition.

Declaration of competing interest

The authors declare the following financial interests/personal relationships which may be considered as potential competing interests: Philip J. Vardon is a member of the Editorial Board of Computers & Geotechnics, but was not involved in the review or decision process. The other authors declare that they have no known competing financial interests or personal relationships that could have appeared to influence the work reported in this paper.

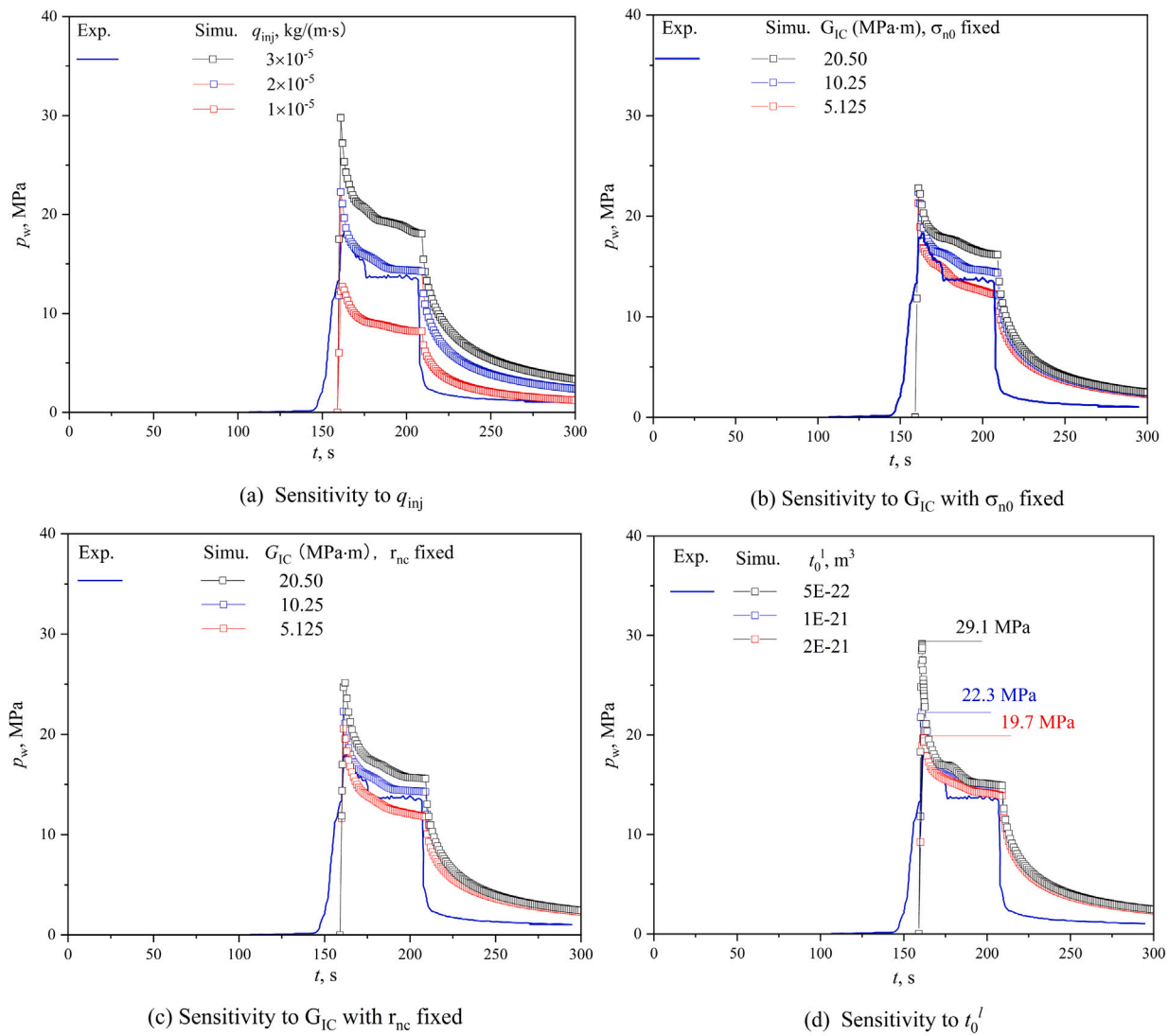


Fig. 15. Sensitivity analysis Model B: the influence of injection rate Q_{inj} , specific fracture energy G_{IC} and the initial longitudinal hydraulic conductivity t_0^l on pressure response.

Acknowledgement

This project has received funding from the European Union's Horizon 2020 research and innovation programme under the Marie Skłodowska-Curie grant agreement No 956965.

Data availability

No data was used for the research described in the article.

References

- Adachi, J.I., Detournay, E., 2002. Self-similar solution of a plane-strain fracture driven by a power-law fluid. *Int. J. Numer. Anal. Met.* 26 (6), 579–604. <http://dx.doi.org/10.1002/nag.213>.
- Akdas, S.B., Onur, M., 2022. Analytical solutions for predicting and optimizing geothermal energy extraction from an enhanced geothermal system with a multiple hydraulically fractured horizontal-well doublet. *Renew. Energ.* 181, 567–580. <http://dx.doi.org/10.1016/j.renene.2021.09.051>.
- Alonso, E.E., Zandarín, M.T., Olivella, S., 2013. Joints in unsaturated rocks: Thermo-hydro-mechanical formulation and constitutive behaviour. *J. Rock Mech. Geotech. Eng.* 5 (3), 200–213. <http://dx.doi.org/10.1016/j.jrmge.2013.05.004>.
- Baiocchi, C., Brezzi, F., Franca, L.P., 1993. Virtual bubbles and Galerkin-least-squares type methods (Ga.L.S.). *Comput. Method Appl. M.* 105 (1), 125–141. [http://dx.doi.org/10.1016/0045-7825\(93\)90119-1](http://dx.doi.org/10.1016/0045-7825(93)90119-1).
- Barenblatt, G.I., 1962. The mathematical theory of equilibrium cracks in brittle fracture. *Adv. Appl. Mech.* 7, 55–129. [http://dx.doi.org/10.1016/S0065-2156\(08\)70121-2](http://dx.doi.org/10.1016/S0065-2156(08)70121-2).
- Barends, F.B.J., 2010. Complete solution for transient heat transport in porous media, following laurier's concept. In: *SPE Annual Technical Conference and Exhibition*. Florence, pp. 19–22. URL: <http://onepetro.org/SPEATCE/proceedings-pdf/10ATCE/All-10ATCE/SPE-134670-MS/1726378/spe-134670-ms.pdf/1>.
- Benson, S.M., Daggett, J.S., Iglesias, E., Arellano, V., Ortiz-Ramirez, J., 1987. Analysis of thermally induced permeability enhancement in geothermal injection wells. In: *12th Workshop on Geothermal Reservoir Engineering*. Stanford, California, URL: <https://www.osti.gov/biblio/888500>.
- Carrier, B., Granet, S., 2012. Numerical modeling of hydraulic fracture problem in permeable medium using cohesive zone model. *Eng. Fract. Mech.* 79, 312–328. <http://dx.doi.org/10.1016/j.engfracmech.2011.11.012>.
- Cerfontaine, B., Dieudonné, A.C., Radu, J.P., Collin, F., Charlier, R., 2015. 3D zero-thickness coupled interface finite element: Formulation and application. *Comput. Geotech.* 69, 124–140. <http://dx.doi.org/10.1016/j.compgeo.2015.04.016>.
- Charlier, R., 1987. *Approche Unifiée de Quelques Problèmes Non Linéaires de Mécanique des Milieux Continus par la Méthode des Éléments Finis (Grandes Déformations des Métaux et des Sols, Contact Unilatéral de Solides, Conduction Thermique et Écoulements en Milieu Poreux)* (Ph.D. thesis). University of Liège, Liège, p. 301.
- Cheng, Y., Zhang, Y., Yu, Z., Hu, Z., Ma, Y., Yang, Y., 2021. Experimental and numerical studies on hydraulic fracturing characteristics with different injection flow rates in granite geothermal reservoir. *Energy Sci. Eng.* 9 (1), 142–168. <http://dx.doi.org/10.1002/ese3.816>.
- Collin, F., 2003. *Couplages Thermo-hydro-mécaniques dans les Sols et les Roches Tendres Partiellement Saturés* (Ph.D. thesis). Université de Liège, Liège, URL: <https://orbi.uliege.be/bitstream/2268/87866/1/PhdCollin.pdf>.

- Collin, F., Li, X.L., Radu, J.P., Charlier, R., 2002. Thermo-hydro-mechanical coupling in clay barriers. *Eng. Geol.* 64 (2–3), 179–193. [http://dx.doi.org/10.1016/S0013-7952\(01\)00124-7](http://dx.doi.org/10.1016/S0013-7952(01)00124-7).
- Cui, W., Potts, D.M., Zdravković, L., Gawecka, K.A., Tsiamposi, A., 2019. Formulation and application of 3D THM-coupled zero-thickness interface elements. *Comput. Geotech.* 116, 103204. <http://dx.doi.org/10.1016/j.compgeo.2019.103204>.
- Dally, T., Bilgen, C., Werner, M., Weinberg, K., 2020. Cohesive elements or phase-field fracture: which method is better for dynamic fracture analyses? In: *Modeling and Simulation in Engineering - Selected Problems*. IntechOpen, <http://dx.doi.org/10.5772/intechopen.92180>.
- Diersch, H.J.G., 2014. *FEFLOW: Finite Element Modeling of Flow, Mass and Heat Transport in Porous and Fracturedmedia*, first ed. Springer Berlin, Heidelberg, pp. 308–319. <http://dx.doi.org/10.1007/978-3-642-38739-5>.
- Dieudonné, A.-C., 2016. *Hydromechanical Behaviour of Compacted Bentonite: From Micro-Scale Analysis to Macro-Scale Modelling* (Ph.D. thesis). Université de Liège, Liège.
- Dieudonné, A.C., Cerfontaine, B., Collin, F., Charlier, R., 2015. Hydromechanical modelling of shaft sealing for CO₂ storage. *Eng. Geol.* 193, 97–105. <http://dx.doi.org/10.1016/j.enggeo.2015.04.016>.
- Dobbie, T.P., Maunder, B.R., Sarit, A.D., 1982. ReInjection experience in the Philippines. In: *New Zealand Geothermal Workshop*. URL: <https://www.geothermal-energy.org/pdf/IGASTandard/NZGW/1982/Dobbie.pdf>.
- Doughty, C., 2013. User's Guide for Hysteretic Capillary Pressure and Relative Permeability Functions in TOUGH2. Technical Report LBNL-6533E, Lawrence Berkeley National Laboratory, Berkeley, California, <http://dx.doi.org/10.2172/1164322>.
- Dudani, N., Bhalla, U.S., Ray, S., 2014. MOOSE, the Multiscale Object-Oriented Simulation Environment. Springer, New York, pp. 1–4. http://dx.doi.org/10.1007/978-1-4614-7320-6_257-1.
- Dugdale, D.S., 1960. Yielding of steel sheets containing slits. *J. Mech. Phys. Solids* 8 (2), 100–104. [http://dx.doi.org/10.1016/0022-5096\(60\)90013-2](http://dx.doi.org/10.1016/0022-5096(60)90013-2).
- European Commission, 2023. Report on geothermal energy. Technical Report 2023/2111(INI), Committee on Industry, Research and Energy, URL: https://www.europarl.europa.eu/doceo/document/A-9-2023-0432_EN.html.
- Fabrizi, H., Sánchez, M., Maedo, M., Cleto, P., Manzoli, O., 2023. Modeling gas breakthrough and flow phenomena through engineered barrier systems using a discrete fracture approach. *Comput. Geotech.* 154, 105148. <http://dx.doi.org/10.1016/j.compgeo.2022.105148>.
- Fallahzadeh, S., Hossain, M., Cornwell, A.J., Rasouli, V., 2017. Near wellbore hydraulic fracture propagation from perforations in tight rocks: The roles of fracturing fluid viscosity and injection rate. *Energies* 10 (3), 359. <http://dx.doi.org/10.3390/en10030359>.
- Fox, D.B., Koch, D.L., Tester, J.W., 2016. An analytical thermohydraulic model for discretely fractured geothermal reservoirs. *Water Resour. Res.* 52 (9), 6792–6817. <http://dx.doi.org/10.1002/2016WR018666>.
- Garipov, T.T., Tomin, P., Rin, R., Voskov, D.V., Tchepeli, H.A., 2018. Unified thermo-compositional-mechanical framework for reservoir simulation. *Comput. Geosci.* 22 (4), 1039–1057. <http://dx.doi.org/10.1007/s10596-018-9737-5>.
- Garolera Vinent, D., 2017. *Zero-Thickness Interface Elements in Petroleum Geomechanics: Sand Production and Hydraulic Fractureproblems* (Ph.D. thesis). Universitat Politècnica de Catalunya · BarcelonaTech, Barcelona, pp. 78–84, URL: <https://upcommons.upc.edu/bitstream/2117/168575/1/TDGV1de1.pdf>.
- Geertsma, J., De Klerk, F., 1969. A rapid method of predicting width and extent of hydraulically induced fractures. *J. Pet. Technol.* 21 (12), 1571–1581. <http://dx.doi.org/10.2118/2458-PA>.
- Grant, M.A., Clearwater, J., Quinão, J., Bixley, P.F., Le Brun, M., 2013. Thermal stimulation of geothermal wells: A review of field data. In: *38th Workshop on Geothermal Reservoir Engineering*. Stanford, California, URL: <https://pangea.stanford.edu/ERE/pdf/IGASTandard/SGW/2013/Grant1.pdf>.
- Gunnarsson, G., 2011. Mastering reinjection in the hellisheidi field, SW-Iceland: A story of successes and failures. In: *36th Workshop on Geothermal Reservoir Engineering*. Stanford, California, URL: <https://pangea.stanford.edu/ERE/pdf/IGASTandard/SGW/2011/gunnarsson1.pdf>.
- Guo, F., Morgenstern, N.R., Scott, J.D., 1993. Interpretation of hydraulic fracturing breakdown pressure. *Int. J. Rock Mech. Min. Sci. Geomech. Abstr.* 30 (6), 617–626. [http://dx.doi.org/10.1016/0148-9062\(93\)91221-4](http://dx.doi.org/10.1016/0148-9062(93)91221-4).
- Heinrich, J.C., Huyakorn, P.S., Zienkiewicz, O.C., Mitchell, A.R., 1977. An 'upwind' finite element scheme for two-dimensional convective transport equation. *Internat. J. Numer. Methods Engrg.* 11 (1), 131–143. <http://dx.doi.org/10.1002/nme.1620110113>.
- Hillerborg, A., Modéer, M., Petersson, P.-E., 1976. Analysis of crack formation and crack growth in concrete by means of fracture mechanics and finite elements. *Cem. Concr. Res.* 6 (6), 773–781. [http://dx.doi.org/10.1016/0008-8846\(76\)90007-7](http://dx.doi.org/10.1016/0008-8846(76)90007-7).
- Horne, R.N., 1982. *Effects of Water Injection into Fractured Geothermal Reservoirs: A Summary of Experience Worldwide*. Technical Report SGP-TR-57, Stanford University, Stanford, California, <http://dx.doi.org/10.2172/860855>.
- Israelsson, J.I., 1996. Short descriptions of UDEC and 3DEC. *Dev. Geotech. Eng.* 79, 523–528. [http://dx.doi.org/10.1016/S0165-1250\(96\)80041-1](http://dx.doi.org/10.1016/S0165-1250(96)80041-1).
- Jacquey, A.B., 2017. *Coupled Thermo-Hydro-Mechanical Processes in Geothermal Reservoirs: A Multiphysics and Multiscale Approach Linking Geology and 3D Numerical Modelling* (Ph.D. thesis). RWTH Aachen, Aachen, <http://dx.doi.org/10.18154/RWTH-2017-09790>.
- Jaeger, J.C., Cook, N.G.W., Zimmerman, R., 2009. *Fundamentals of Rock Mechanics*, 4th ed. Wiley-Blackwell, pp. 197–203.
- Jafari, A., Vahab, M., Broumand, P., Khalili, N., 2023. An extended finite element method implementation in COMSOL multiphysics: Thermo-hydro-mechanical modeling of fluid flow in discontinuous porous media. *Comput. Geotech.* 159, 103707. <http://dx.doi.org/10.1016/j.compgeo.2023.105458>.
- Khrstianovic, S.A., Zheltov, Y.P., 1955. Formation of vertical fractures by means of highly viscous liquid. In: *The 4th World Petroleum Congress*. Rome, URL: <http://onepetro.org/WPCONGRESS/proceedings-pdf/WPC04/All-WPC04/WPC-6132/2082397/wpc-6132.pdf/1>.
- Kikuchi, N., 1982. A smoothing technique for reduced integration penalty methods in contact problems. *Internat. J. Numer. Methods Engrg.* 18 (3), 343–350. <http://dx.doi.org/10.1002/nme.1620180303>.
- Kolditz, O., Bauer, S., Bilke, L., Böttcher, N., Delfs, J.O., Fischer, T., Görke, U.J., Kalbacher, T., Kosakowski, G., McDermott, C.I., Park, C.H., Radu, F., Rink, K., Shao, H., Shao, H.B., Sun, F., Sun, Y.Y., Singh, A.K., Taron, J., Walther, M., Wang, W., Watanabe, N., Wu, Y., Xie, M., Xu, W., Zehner, B., 2012. OpenGeoSys: An open-source initiative for numerical simulation of thermo-hydro-mechanical/chemical (THM/C) processes in porous media. *Env. Earth Sci.* 67 (2), 589–599. <http://dx.doi.org/10.1007/s12665-012-1546-x>.
- Krogstad, S., Lie, K.A., Møyner, O., Nilsen, H.M., Raynaud, X., Skaflestad, B., 2015. MRST-AD - an open-source framework for rapid prototyping and evaluation of reservoir simulation problems. In: *2015 SPE Reservoir Simulation Symposium*. vol. 3, Society of Petroleum Engineers, Houston, Texas, pp. 2080–2105. <http://dx.doi.org/10.2118/173317-ms>.
- Lauwerier, H.A., 1955. The transport of heat in an oil layer caused by the injection of hot fluid. *J. Appl. Sci. Res.* 5 (2–3), 145–150.
- Lei, Q., Barton, N., 2022. On the selection of joint constitutive models for geomechanics simulation of fractured rocks. *Comput. Geotech.* 145, 104707. <http://dx.doi.org/10.1016/j.compgeo.2022.104707>.
- Lepillier, B., Yoshioka, K., Parisio, F., Bakker, R., Bruhn, D., 2020. Variational phase-field modeling of hydraulic fracture interaction with natural fractures and application to enhanced geothermal systems. *J. Geophys. Res. Solid Earth* 125 (7), <http://dx.doi.org/10.1029/2020JB019856>.
- Lequesne, C., Plumier, A., Degee, H., Habraken, A.M., 2006. Numerical study of the fatigue crack in welded beam-to-column connection using cohesive zone model. *Key Eng. Mater.* 324–325, 847–850. <http://dx.doi.org/10.4028/www.scientific.net/kem.324-325.847>.
- Liaudat, J., Dieudonné, A.-C., Vardon, P.J., 2023. Modelling gas fracturing in saturated clay samples using triple-node zero-thickness interface elements. *Comput. Geotech.* 154, 105128. <http://dx.doi.org/10.1016/j.compgeo.2022.105128>.
- Livermore Software Technology, 2007. LS-DYNA® keyword user's manual: Volume i. URL: www.lstc.com.
- Lu, Y.L., Elsworth, D., Wang, L.G., 2013. Microcrack-based coupled damage and flow modeling of fracturing evolution in permeable brittle rocks. *Comput. Geotech.* 49, 226–244. <http://dx.doi.org/10.1016/j.compgeo.2012.11.009>.
- Luo, W., Kottsova, A., Vardon, P.J., Dieudonné, A.C., Brehme, M., 2023. Mechanisms causing injectivity decline and enhancement in geothermal projects. *Renew. Sustain. Energy Rev.* 185, 113623. <http://dx.doi.org/10.1016/j.rser.2023.113623>.
- Mi, Y., Crisfield, M.A., Davies, G.A.O., Hellweg, H.B., 1998. Progressive delamination using interface elements. *J. Compos. Mater.* 32 (14), 1246–1272. <http://dx.doi.org/10.1177/002199839803201401>.
- Min, K., 2013. *Numerical Modelling of Hydraulic Fracture Propagation Using Thermo-Hydro-Mechanical Analysis with Brittle Damage Model by Finite Element Method* (Ph.D. thesis). Texas A & M University, College Station, Texas, URL: <https://hdl.handle.net/1969.1/150961>.
- Nguyen, V.P., Lian, H., Rabczuk, T., Bordas, S., 2017. Modelling hydraulic fractures in porous media using flow cohesive interface elements. *Eng. Geol.* 225, 68–82. <http://dx.doi.org/10.1016/j.enggeo.2017.04.010>.
- Owen, A., 1984. Artificial diffusion in the numerical modelling of the advective transport of salinity. *Appl. Math. Model.* 8 (2), 116–120. [http://dx.doi.org/10.1016/0307-904X\(84\)90063-5](http://dx.doi.org/10.1016/0307-904X(84)90063-5).
- Pérez Carreras, A., 2018. *T-H-M coupling with large advection in fractured rock masses using zero-thickness interface elements* (Ph.D. thesis). Universitat Politècnica de Catalunya · BarcelonaTech, Barcelona, URL: <http://hdl.handle.net/2117/341611>.
- Podgorny, R., Finnilla, A., Simmons, S., McLennan, J., 2021. A reference thermal-hydro-mechanical native state model of the Utah FORGE enhanced geothermal site. *Energies* 14 (16), 4758. <http://dx.doi.org/10.3390/en14164758>.
- Ranjbar, A., Hassani, H., Shahriar, K., Shahriar, M.J.A., 2020. Thermo-hydro-mechanical modeling of fault discontinuities using zero-thickness interface element. *J. Rock Mech. Geotech. Eng.* 12 (1), 74–88. <http://dx.doi.org/10.1016/j.jrmge.2019.05.005>.
- Scheider, I., 2001. Cohesive model for crack propagation analyses of structures with elastic-plastic material behavior foundations and implementation. URL: https://www.climate-service.info/imperia/md/content/gkss/institut_fuer_werkstofforschung/wms/czm-doku.pdf.
- Schrefler, B.A., Secchi, S., Simoni, L., 2006. On adaptive refinement techniques in multi-field problems including cohesive fracture. *Comput. Method Appl. M.* 195 (4–6), 444–461. <http://dx.doi.org/10.1016/j.cma.2004.10.014>.

- Settgast, R., 2022. GEOSX documentation. pp. 173–179, URL: <https://geosx-geosx.readthedocs-hosted.com/en/latest/>.
- Settgast, R.R., Fu, P., Walsh, S.D., White, J.A., Annavarapu, C., Ryerson, F.J., 2017. A fully coupled method for massively parallel simulation of hydraulically driven fractures in 3-dimensions. *Int. J. Numer. Anal. Met.* 41 (5), 627–653. <http://dx.doi.org/10.1002/nag.2557>.
- Spence, D.A., Sharp, P., 1985. Self-similar solutions for elastohydrodynamic cavity flow. *Proc. R. Soc. Lond.* 400 (1819), 289–313. <http://dx.doi.org/10.1098/rspa.1985.0081>.
- Valkó, P., Economides, M.J., 1995. *Hydraulic Fracture Mechanics*. Wiley.
- Van Den Bogert, P.A.J., 2015. *Impact of Various Modelling Options on the Onset of Fault Slip and the Fault Slip Response Using 2-Dimensional Finite-Element Modelling*. Technical Report SR.15.11455, Shell.
- Veldkamp, J.G., Loeve, D., Peters, E., Nair, R., Pizzocolo, F., 2016. Thermal fracturing due to low injection temperatures in geothermal doublets. Technical Report TNO 2015 R11739, TNO, Utrecht, URL: www.tno.nl.
- Wang, Y., Voskov, D., Khait, M., Bruhn, D., 2020. An efficient numerical simulator for geothermal simulation: A benchmark study. *Appl. Energ.* 264, 114693. <http://dx.doi.org/10.1016/j.apenergy.2020.114693>.
- Wu, J.-Y., Nguyen, V.P., Nguyen, C.T., Sutula, D., Sinaie, S., Bordas, S.P., 2020. Phase-field modeling of fracture. *Adv. Appl. Mech.* 53, 1–183. <http://dx.doi.org/10.1016/bs.aams.2019.08.001>.
- Zhang, W., Guo, T.K., Qu, Z.Q., Wang, Z.Y., 2019. Research of fracture initiation and propagation in HDR fracturing under thermal stress from meso-damage perspective. *Energy* 178, 508–521. <http://dx.doi.org/10.1016/j.energy.2019.04.131>.
- Zhuang, L., Kim, K.Y., Jung, S.G., Diaz, M., Min, K.-B., 2019. Effect of water infiltration, injection rate and anisotropy on hydraulic fracturing behavior of granite. *Rock Mech. Rock Eng.* 52 (2), 575–589. <http://dx.doi.org/10.1007/s00603-018-1431-3>.
- Zimmerman, R.W., Yeo, I.-W., 2000. Fluid flow in rock fractures: From the Navier-Stokes equations to the cubic law. In: *Dynamics of Fluids in Fractured Rock*. vol. 122, Wiley, pp. 213–224. <http://dx.doi.org/10.1029/GM1222p0213>.
- Zyvoloski, G., 2007. FEHM: A Control Volume Finite Element Code for Simulating Subsurface Multi-Phase Multi-Fluid Heat and Mass Transfer. Technical Report LAUR-07-3359, Los Alamos National Laboratory, Los Alamos, New Mexico, URL: https://www.lanl.gov/orgs/ees/fehm/pdfs/FEHM_LAUR-07-3359.pdf.